# Theory of single-charge exchange heavy-ion reactions

Horst Lenske,[1,*] Jessica I. Bellone,[2,3,†] Maria Colonna,[2,‡] and José-Antonio Lay[2,4,§]
(NUMEN Collaboration)
[1]*Institut für Theoretische Physik, Justus-Liebig-Universität Giessen, D-35392 Giessen, Germany*
[2]*INFN-LNS, I-95123 Catania, Italy*
[3]*Dipartimento di Fisica e Astronomia, Universitá degli studi di Catania, Italy*
[4]*Departamento de FAMN, Universidad de Sevilla, Apartado 1065, E-41080 Sevilla, Spain*

(Received 16 February 2018; revised manuscript received 27 August 2018; published 24 October 2018)

The theory of heavy-ion single-charge exchange reactions is reformulated. In momentum space, the reaction amplitude factorizes into a product of projectile and target transition form factors, folded with the nucleon-nucleon isovector interaction. The multipole structure of the transition form factors is studied in detail for Fermi-type non-spin-flip and Gamow-Teller-type spin-flip transitions, also serving to establish the connection to nuclear $\beta$ decay. The reaction kernel is evaluated for central and rank-2 tensor interactions. Initial- and final-state ion-ion elastic interactions are accounted for by a distortion coefficient. Since the ion-ion interactions are dominated by the imaginary part of the optical potentials, the distortion coefficients can be evaluated in the strong absorption limit. For a Gaussian potential form factor, the distortion coefficient is evaluated in closed form, revealing the relation to the total reaction cross section. It is shown that at small momentum transfer distortion effects reduce to a simple scaling factor, allowing us to define a reduced forward-angle cross section which is given by nuclear matrix elements of $\beta$ decay type. Thus we introduce new unit cross sections, as those traditionally used with light projectiles for spectroscopic purposes, for heavy-ion charge-exchange reactions. Results are discussed for $\tau_{\pm}$ excitations of $^{18}$O and $^{40}$Ca, respectively. Spectral distributions of nuclear-charge-changing transitions are obtained by self-consistent Hartree-Fock-Bogolubov (HFB) and quasiparticle random phase approximation (QRPA) theory and compared to spectroscopic data. The interplay of nuclear structure and reaction dynamics is illustrated for the single-charge exchange (SCE) reaction $^{18}\mathrm{O} + {}^{40}\mathrm{Ca} \rightarrow {}^{18}\mathrm{F} + {}^{40}\mathrm{K}$ at $T_{\mathrm{lab}} = 270$ MeV, by performing full-scale numerical calculations of the SCE cross section. We also show that the latter compare rather well with the results obtained within the strong absorption limit, thus confirming the possibility to factorize the forward-angle cross section into intrinsic nuclear transition dynamics and reaction dynamics.

DOI: 10.1103/PhysRevC.98.044620

## I. INTRODUCTION

Nuclear charge exchange reactions have been the major source of information on the isospin and spin-isospin modes of excitation in nuclei. The discovery of the giant Gamow-Teller resonance (GTR) by the pioneering experiments at IUCF [1] initiated widespread experimental and theoretical research activities, continuing with increasing intensity until today. Over the years, a wealth of data has been accumulated as reviewed, e.g., in [2–6]. Beyond using nucleonic probes, light-ion reactions as, e.g., ($^3$He, $^3$H) have become another workhorse of the field, now reaching accuracies that allow us to investigate subtle details of spectral distributions in both the $\tau_+$ and the $\tau_-$ branches. Soon after the first light-ion studies, heavy ions were used in charge exchange studies as in Refs. [7,8]. It was recognized that peripheral heavy-ion collisions, leading to direct reactions, are as useful for spectral studies as light-ion scattering. An especially appealing aspect is the broad range of projectile-target combinations which, for example, allow us to project out selectively specific features, e.g., spin-flip and non-spin-flip transitions [9]. Nuclear spin dynamics and the population of continuum states were central aspects of the ($^7$Be, $^7$Li) reactions considered in Refs. [10,11]. While the past experiments have been focused on single-charge exchange (SCE) reactions, new territory was entered with the pilot experiment of Cappuzzello *et al.* [12], which studied a nuclear double-charge exchange (DCE) reaction. The reaction $^{18}\mathrm{O} + {}^{40}\mathrm{Ca} \rightarrow {}^{18}\mathrm{Ne} + {}^{40}\mathrm{Ar}$ gave strong evidence for a direct reaction mechanism even for double-charge exchange processes. Quite recently, the NUMEN project at LNS Catania was initiated, dedicated to investigations of SCE and DCE heavy-ion reactions that elucidate and optimize their potential for spectroscopic studies [13].

On the theoretical side, light-ion reactions have attracted the greatest attention. SCE reactions are typically well described by the distorted-wave Born approximation (DWBA) methods in conjunction with microscopic nuclear structure input. A comprehensive and still widely used formulation of light-ion SCE reactions was worked out by Taddeucci *et al.* [14], focusing on the spectroscopic applications. DWBA

*horst.lenske@theo.physik.uni-giessen.de
†jessica.bellone@ct.infn.it
‡colonna@lns.infn.it
§lay@us.es

 

methods and microscopic nuclear structure input are also essential for the quantitative description of heavy-ion SCE reactions. Spectral results from shell model and quasiparticle random phase approximation (QRPA) calculations were indeed used already from the beginning, for example, in Refs. [7–9] and also in the later investigations in Refs. [10,11]. An important difference between light- and heavy-ion collisions lies in the reaction mechanism. In principle, heavy-ion SCE reactions are proceeding by two competing reaction mechanisms. The direct SCE process is a collisional process, mediated by the exchange of charged mesons between projectile and target, as given by the isovector nucleon-nucleon interaction. Hence, the direct SCE reaction mechanism is probing directly the isospin structure of the ions. A competing reaction mechanism is the sequential exchange of protons and neutrons. This is at least a second-order process, mainly probing the mean-field structure of the ions. In Refs. [7,9,15], the two reaction scenarios have been discussed. Direct SCE provides access to nuclear transition matrix elements with spin-isospin vertices as in weak interaction $\beta$ decay. This is not the case for the transfer SCE mechanism. By a proper choice of projectile and target, however, the transfer branch can be suppressed. In this paper, we consider only the theory of collisional direct SCE reactions.

In heavy-ion scattering above the Coulomb barrier, a large number of reaction channels are available, absorbing a considerable part of the incoming flux. Thus, heavy-ion SCE reactions occur in a strongly absorptive environment, although the SCE cross sections are a minor contribution to the total reaction cross section. As any direct nuclear reaction, peripheral heavy-ion charge exchange processes incorporate reaction and nuclear structure dynamics. Both aspects are intimately interwoven and require their own specific theoretical treatment.

In this paper, we present a concise formulation of the theory. For the reaction part, our guiding principle is direct nuclear reaction theory. In Sec. II, we recapitulate the theory of charge exchange reactions, based on the distorted-wave Born approximation (DWBA). Initial- and final-state ion-ion interactions are described by optical potentials. Microscopic optical potentials are used, obtained in the impulse approximation, by folding projectile and target Hartree-Fock-Bogolubov (HFB) ground-state densities with free space nucleon-nucleon $T$ matrices. In this way, we overcome the lack of elastic scattering data, inhibiting the determination of empirical optical potentials. Until the availability of elastic scattering data, we are left, however, with an open flank of unchecked input. Special emphasis is laid on a suitable formulation of the residual ion-ion charge exchange interaction. We show that momentum representation is of special advantage, allowing us to separate the interaction into operators acting in projectile and target, respectively. We include central rank-0 and rank-2 tensor interactions. It is shown that these two types of interactions can be represented by the same set of operators. Expressions for the reaction amplitudes and differential cross sections are derived.

In Sec. III, the intrinsic nuclear operators are evaluated in second quantization, leading to a representation of the residual ion-ion interaction in terms of one-body density operators. Thus, we arrive at a formulation treating interactions and form factors in the general scheme of second quantization, independent of a particular nuclear structure model. The model dependence is introduced only at the very end of the theoretical process when the one-body density matrices have to be evaluated with respect to specific nuclear wave functions. The relation of the form factor and SCE reaction amplitudes to nuclear $\beta$ decay is clarified by considering the limit of low momentum transfer. The momentum space techniques are found to provide the proper approach to disentangle reaction and structure aspects. In heavy-ion SCE reactions, also the projectile may have a number of bound excited states, requiring to consider the combined spectral distributions of both ions. Finally, we derive explicit expressions for forward angle cross sections, showing that heavy-ion SCE reactions are indeed providing access to nuclear matrix elements relevant also for $\beta$ decay. The results derived in this section are of special importance since they show explicitly the potential of heavy-ion SCE reactions for spectral investigations, including the deduction of nuclear matrix elements for $\beta$ decay.

Section IV as a central part of the paper is concerned with the investigation of initial- and final-state interactions. They are of crucial importance for an understanding of the reaction yields on a quantitative level. Their effect is, of course, treated properly on the quantum mechanical level by direct reaction theory. However, in order to disentangle SCE reaction dynamics and nuclear dynamics, a deeper insight into elastic ion-ion interactions is necessary. For that purpose, the momentum space formulation of the reaction amplitude is of great advantage. The final result is surprisingly simple: The main effect of ion-ion elastic interactions is finally to act as a (momentum-dependent) weight factor in the folding of the nuclear transition form factors, suitably described by a distortion coefficient. The latter is found to be closely related to the elastic optical model $S$ matrix. In the strong absorption limit, analytic expressions are derived in Gaussian approximation for the transition potentials in Sec. IV C. In leading order, elastic ion-ion interactions reduce to a simple scaling law, suppressing, however, the SCE cross section by many orders of magnitude with respect to the plane-wave Born limit. SCE reactions in the strong absorption limit and an interesting connection to eikonal theory is discussed in Sec. V.

Last but not least, the theoretical results are illustrated in Sec. VI by numerical calculations. QRPA results for nuclear SCE response functions are presented for $^{18}\mathrm{O} \rightarrow {}^{18}\mathrm{F}$ and $^{40}\mathrm{Ca} \rightarrow {}^{40}\mathrm{K}$, respectively. We discuss results for optical potentials and elastic scattering angular distributions, addressing distortion effects due to ion-ion dynamics and examples of charge exchange cross sections. As a case of physical interest, we consider throughout the SCE reaction $^{18}\mathrm{O} + {}^{40}\mathrm{Ca} \rightarrow {}^{18}\mathrm{F} + {}^{40}\mathrm{K}$ at $T_{\mathrm{lab}} = 15$ A MeV. Mathematical-theoretical details have been shifted into a few appendices. The paper closes in Sec. VII with a summary and an outlook for future work.

## II. THEORY OF HEAVY-ION SINGLE-CHARGE EXCHANGE REACTIONS

Charge-changing reactions by strong interactions are off-shell processes mediated by the exchange of virtual particles.

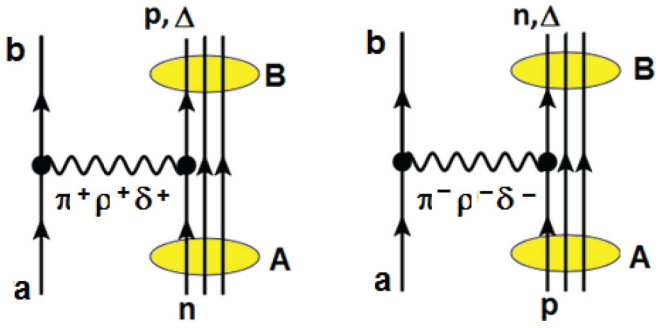


FIG. 1. Graphical representation of a single-charge exchange heavy-ion reaction by hadronic interactions corresponding to $\nu\beta$ processes. Both $(n, p)$-type (left) and $(p, n)$-type (right) reactions, as seen in the $A \to B$ transition in target system, are displayed, indicating also the exchanged meson.

They require two reaction partners, which are acting mutually as the source or sink, respectively, of the charge-changing virtual meson fields, as depicted in Fig. 1. For experimental reasons, the projectile-like ejectile should be preferentially in a particle-stable state (see, however, $(d, {}^2\mathrm{He})$ reactions [16]), thus simplifying the detection. If the ejectile has only a single bound state below the particle emission threshold, the calculations and the interpretation of the spectroscopic data are especially simple.

Here, we consider ion-ion SCE reactions according to

$$ {}^{a}_{z}a + {}^{A}_{Z}A \to {}^{a}_{z\pm1}b + {}^{A}_{Z\mp1}B, \tag{1}$$

which change the charge partition by a balanced redistribution of protons and neutrons.

The differential SCE cross section for a reaction connecting the channels $\alpha$ and $\beta$ is defined as

$$ d2\sigma_{\alpha\beta} = \frac{m_\alpha m_\beta}{(2\pi\hbar^2)^2}\frac{k_\beta}{k_\alpha}\frac{1}{(2J_a+1)(2J_A+1)} \times \sum_{M_a,M_A\in\alpha;M_b,M_B\in\beta} |M_{\alpha\beta}(\mathbf{k}_\alpha,\mathbf{k}_\beta)|^2 d\Omega, \tag{2}$$

where $\mathbf{k}_\alpha$ ($\mathbf{k}_\beta$) and $m_\alpha$ ($m_\beta$) denote the relative 3-momentum and reduced mass in the entrance (exit) channel $\alpha = \{a, A\}$ ($\beta = \{b, B\}$). $\{J_a M_a, J_A M_A \ldots\}$ and $\{J_b M_b, J_B M_B \ldots\}$ account for the full set of (intrinsic) quantum numbers specifying the initial and final channel states, respectively.

In the distorted-wave approximation, the direct charge exchange reaction amplitude is given by the expression

$$ M_{\alpha\beta}(\mathbf{k}_\beta,\mathbf{k}_\alpha) = \langle \chi^{(-)}_\beta, bB|T_{NN}|aA, \chi^{(+)}_\alpha\rangle. \tag{3}$$

The distorted waves, denoted by $\chi^{(\pm)}_{\alpha,\beta}$ for asymptotically outgoing and incoming spherical waves, respectively, depend on the respective channel momenta $\mathbf{k}_{\alpha,\beta}$ and the optical potentials, thus accounting for initial-state (ISI) and final-state (FSI) interactions.

The charge-changing process is described by the nucleon-nucleon ($NN$) $T$ matrix $T_{NN}$. Antisymmetrization between target and projectile nucleons is taken care of by the standard procedure of attaching the spin and isospin exchange operators to the $T$ matrix and treating space exchange in local momentum approximation; see, e.g., Refs. [17–19]. The antisymmetrized $T$ matrix is then given in nonrelativistic momentum representation by

$$ T_{NN}(\mathbf{p}) = \sum_{S=0,1,T=0,1} \{V^{(C)}_{\mathrm{ST}}(p^2)[\boldsymbol{\sigma_a}\cdot\boldsymbol{\sigma_B}]^S + \delta_{S1}V^{(Tn)}_T(p^2)S_{12}(\mathbf{p})[\boldsymbol{\tau}_a\cdot\boldsymbol{\tau}_A]^T\}, \tag{4}$$

including isoscalar and isovector central spin-independent ($S = 0$) and spin-dependent ($S = 1$) interactions with form factors $V^{(C)}_{\mathrm{ST}}(p^2)$, respectively, and rank-2 tensor interactions with form factors $V^{(Tn)}_T(p^2)$. The form factors are complex-valued scalar functions. Denoting the nucleon isospinors by $|p\rangle$ and $|n\rangle$, respectively, we use the convention $\langle p|\tau_0|p\rangle = +1$, which implies $\tau_-|p\rangle = |n\rangle$. The standard definition of the rank-2 tensor operator is

$$ S_{12}(\mathbf{p}) = \frac{1}{p^2}(3\boldsymbol{\sigma}_a\cdot\mathbf{p}\,\boldsymbol{\sigma}_A\cdot\mathbf{p} - \boldsymbol{\sigma}_a\cdot\boldsymbol{\sigma}_A p^2), \tag{5}$$

but for applications to nuclear reactions an equivalent, more suitable representation is used, given by the scalar product of two rank-2 tensors, namely the spherical harmonic $Y_{2M}(\hat{\mathbf{p}})$ and the rank-2 spin operator

$$ S_{2M} = [\boldsymbol{\sigma_1}\otimes\boldsymbol{\sigma_2}]_{2M} = \sum_{m_1 m_2}(1m_1 1m_2|2M)\sigma_{1m_1}\sigma_{2m_2} \tag{6}$$

such that

$$ S_{12} = \sqrt{\frac{24\pi}{5}}Y_2 S_2 = \sqrt{\frac{24\pi}{5}}\sum_M Y^*_{2M}(\hat{\mathbf{p}})S_{2M}, \tag{7}$$

where $Y^*_{2M} = (-)^M Y_{2-M}$. For the present discussion, we neglect two-body spin-orbit interactions in order not to overload the presentation.

An elegant representation of the $T$ matrix is obtained in terms of the spin-isospin operators

$$ O_{\mathrm{ST}}(i) = (\boldsymbol{\sigma}_i)^S(\boldsymbol{\tau}_i)^T, \tag{8}$$

which describe the operator structures of both the central and tensor interactions. The operators $O_{\mathrm{ST}}$ lead to the rather compact representation

$$ T_{NN}(\mathbf{p}) = \sum_{S,T}\left\{V^{(C)}_{\mathrm{ST}}(p^2)O_{\mathrm{ST}}(1)O_{\mathrm{ST}}(2) + \delta_{S1}V^{(Tn)}_T(p^2) \times\sqrt{\frac{24\pi}{5}}Y^*_2(\hat{\mathbf{p}})\cdot[O_{\mathrm{ST}}(1)\otimes O_{\mathrm{ST}}(2)]_2\right\}, \tag{9}$$

where scalar products are indicated as dot products and the rank-2 tensorial coupling affects, of course, only the spin degrees of freedom. The subset of isovector operators, corresponding to Fermi-type $S = 0$, $T = 1$ and Gamow-Teller-type $S = 1$, $T = 1$ operators, contributes to the charge-changing reaction amplitudes.

The matrix element of a single-charge exchange reaction, Eq. (1), can be written in slightly different form as

$$ M_{\alpha\beta}(\mathbf{k}_\alpha,\mathbf{k}_\beta) = \langle\chi^{(-)}_\beta|\mathcal{U}_{\alpha\beta}|\chi^{(+)}_\alpha\rangle. \tag{10}$$

The nuclear structure information on multipolarities, transition strength, and interactions are contained in the (antisymmetrized) transition potential

$$\mathcal{U}_{\alpha\beta}(\mathbf{r}_\alpha, \mathbf{r}_\beta) = \langle J_b M_b J_B M_B | T_{NN}^{(C)} + T_{NN}^{(Tn)} ... | J_a M_a J_A M_A \rangle \tag{11}$$

depending on the channel coordinates $\mathbf{r}_{\alpha,\beta}$. If recoil effects due to the change of the mass partitions can be neglected and antisymmetrization is taken into account by an equivalent effective local interaction, one can just consider the local transition potential $\mathcal{U}_{\alpha\beta}(\mathbf{r})$, where $\mathbf{r} = \mathbf{r}_\alpha = \mathbf{r}_\beta$. Obviously, by means of Eq. (11), the reaction amplitude, Eq. (10) can be rewritten in terms of a sum of reaction amplitudes defined by the tensorial rank $\mathfrak{r}$ of the $NN$ interaction,

$$\begin{aligned} M_{\alpha\beta}(\mathbf{k}_\alpha, \mathbf{k}_\beta) &= M_{\alpha\beta}^{(C)}(\mathbf{k}_\alpha, \mathbf{k}_\beta) + M_{\alpha\beta}^{(Tn)}(\mathbf{k}_\alpha, \mathbf{k}_\beta) + \cdots \\ &= \sum_{\mathfrak{r}=C,Tn...} M_{\alpha\beta}^{(\mathfrak{r})}(\mathbf{k}_\alpha, \mathbf{k}_\beta). \end{aligned} \tag{12}$$

## III. SCE CROSS SECTION AND NUCLEAR MATRIX ELEMENTS

### A. Momentum representation

In order to obtain a deeper insight into the interplay of nuclear structure and $\beta$-decay matrix elements on the one side and heavy-ion reaction dynamics on the other side, a more detailed study of the process is necessary. A convenient approach is to consider the reaction amplitude in momentum representation. A considerable advantage of that representation is that the transition potential $\mathcal{U}_{\alpha\beta}$ becomes separable into target and projectile transition form factors. The intrinsic nuclear transitions in either target or projectile are induced by one-body operators of the type

$$\mathcal{R}_{\mathrm{ST}}(\mathbf{p}, \mathbf{r}) = \frac{1}{4\pi} e^{i\mathbf{p}\cdot\mathbf{r}} O_{\mathrm{ST}}, \tag{13}$$

where $\mathbf{r} = \mathbf{r}_{A,a}$ indicates the intrinsic target and projectile nuclear coordinates, respectively. For convenience, we have introduced a normalization to the surface area of the unit sphere. Transitions $X \to Y$ are described by the momentum space form factors

$$F_{\mathrm{ST}}^{(XY)}(\mathbf{p}) = \langle J_Y M_Y | \mathcal{R}_{\mathrm{ST}}(\mathbf{p}, \mathbf{r}_X) | J_X M_X \rangle. \tag{14}$$

The form factors contain the full spectroscopic information on the intrinsic nuclear transitions. In Appendix A, second quantization is used to derive explicit expressions in terms of one-body transition densities.

The reaction kernel is given by products of these form factors

$$\begin{aligned} K_{\alpha\beta}^{(ST)}(\mathbf{p}) = (4\pi)^2 \Big\{ & V_{\mathrm{ST}}^{(C)}(p^2) F_{\mathrm{ST}}^{(ab)\dagger}(\mathbf{p}) \cdot F_{\mathrm{ST}}^{(AB)}(\mathbf{p}) \\ & + \delta_{S1} \sqrt{\frac{24\pi}{5}} V_{\mathrm{ST}}^{(Tn)}(p^2) Y_2^*(\hat{\mathbf{p}}) \\ & \cdot \left[ F_{\mathrm{ST}}^{(ab)\dagger}(\mathbf{p}) \otimes F_{\mathrm{ST}}^{(AB)}(\mathbf{p}) \right]_2 \Big\}, \end{aligned} \tag{15}$$

where the rank-2 tensorial coupling relates to the spin degrees of freedom only. In the central interaction part, the scalar product indicates the contraction of the projectile and target form factor with respect to the spin and isospin degrees of freedom. The isospin degrees of freedom are, of course, projected by the nuclear transitions to the proper combination of $\tau_\pm$ operators. In terms of the reaction kernels, the transition potential is found as

$$\mathcal{U}_{\alpha\beta}(\mathbf{p}) = \sum_{\mathrm{ST}} K_{\alpha\beta}^{(ST)}(\mathbf{p}). \tag{16}$$

It remains to evaluate the integration over the relative motion degrees of freedom, i.e., taking matrix elements with distorted waves. Thus,

$$M_{\alpha\beta}(\mathbf{k}_\alpha, \mathbf{k}_\beta) = \int \frac{d^3p}{(2\pi)^3} \langle \chi_\beta^{(-)} | e^{-i\mathbf{p}\cdot\mathbf{r}} \mathcal{U}_{\alpha\beta}(\mathbf{p}) | \chi_\alpha^{(+)} \rangle \tag{17}$$

and by defining the distortion coefficient

$$N_{\alpha\beta}(\mathbf{k}_\alpha, \mathbf{k}_\beta, \mathbf{p}) = \frac{1}{(2\pi)^3} \langle \chi_\beta^{(-)} | e^{-i\mathbf{p}\cdot\mathbf{r}} | \chi_\alpha^{(+)} \rangle, \tag{18}$$

which will be discussed in detail below in Sec. IV, we obtain the full reaction amplitude

$$M_{\alpha\beta}(\mathbf{k}_\alpha, \mathbf{k}_\beta) = \int d^3p \, \mathcal{U}_{\alpha\beta}(\mathbf{p}) N_{\alpha\beta}(\mathbf{k}_\alpha, \mathbf{k}_\beta, \mathbf{p}), \tag{19}$$

showing the dressing of the nuclear transition potential by initial- and final-state ion-ion interactions. Formally, the above relation is fully equivalent to the DWBA amplitude in coordinate space. The momentum representation, however, has the important advantage that the intrinsic nuclear transition dynamics and the reaction dynamics appear in factorized form.

The projectile and target transition form factors, Eq. (14), are of a very general structure accounting for the complete set of multipoles as contained in the plane waves. The integration over the nuclear intrinsic coordinates, however, will project on a subset of multipoles according to the multipolarity of the transitions $a \to b$ and $A \to B$, respectively.

A special feature is encountered in the rank-2 tensor amplitudes $M_{\alpha\beta}^{(Tn)}$ as discussed, e.g., Ref. [9]. By evaluating the integrals explicitly, one finds that the presence of the spherical harmonics of order 2 induces a corresponding rank-2 tensorial coupling of the nuclear transition multipoles, Eq. (15). Except for transitions involving only $s$-wave proton and neutron orbitals, Gamow-Teller-like excitations are typically a mixture of a leading multipolarity $L_1$ and a subleading one with $L_2 = |L_1 \pm 2|$. $\beta$ decay strongly favors the multipolarity with the lower value of $L_{1,2}$. That selectivity is missing in strong interactions. Since in heavy-ion charge exchange reactions especially processes with large angular momentum transfer are favored, the whole spectrum of multipolarities becomes visible.

The recoupling procedure, following standard rules [20] and discussed in Appendix B, leads to the reduced form factors $F_{LS}^{J_1 J_2}$ and $H_{LS}^{J_1 J_2}$ for central and tensor interactions, respectively. Both are scalar functions of $p^2$; $J_{1,2}$ denote the total angular momentum transfer in projectile and target, respectively; $L$ is the total orbital momentum transfer seen

on the reaction $\alpha \to \beta$, and $S = 0, 1$ indicates as before the spin structure of the transitions. These form factors determine the multipole structure observed in angular distributions. In general, they are given by superpositions of target and projectile intrinsic form factors, as already evident from Eq. (15). Anticipating the result, the reaction kernels become

$$K^{(ST)}_{\alpha\beta}(\mathbf{p}) = \sum_{J_1M_1,J_2M_2,LM} (J_aM_aJ_bM_b|J_1M_1)(J_AM_AJ_BM_B|J_2M_2)(J_1M_1J_2M_2|LM)i^L Y_{LM}(\hat{\mathbf{p}}) \times \left[V^{(C)}_{\rm ST}(p^2)F^{J_1J_2}_{LS}(p^2) + \delta_{S1}V^{(Tn)}_{T}(p^2)H^{J_1J_2}_{LS}(p^2)\right], \tag{20}$$

including central and rank-2 tensor interactions. Correspondingly, for the reaction amplitude, we obtain the expression

$$M_{\alpha\beta}(\mathbf{k}_\alpha, \mathbf{k}_\beta) = \sum_{J_1M_1,J_2M_2,LM} (J_aM_aJ_bM_b|J_1M_1)(J_AM_AJ_BM_B|J_2M_2)(J_1M_1J_2M_2|LM) \times \int d^3p N_{\alpha\beta}(\mathbf{k}_\alpha, \mathbf{k}_\beta, \mathbf{p}) i^L Y_{LM}(\hat{\mathbf{p}}) M^{(J_aJ_A,J_bJ_B)}_{LJ_1J_2}(p^2), \tag{21}$$

where

$$M^{(J_aJ_A,J_bJ_B)}_{LJ_1J_2}(p^2) = \sum_{S,T} \delta_{T1}\left[V^{(C)}_{\rm ST}(p^2)F^{J_1J_2}_{LS}(p^2) + \delta_{S1}V^{(Tn)}_{T}(p^2)H^{J_1J_2}_{LS}(p^2)\right]. \tag{22}$$

Exploiting the completeness and orthogonality relations of Clebsch-Gordan coefficients, the double-differential cross section becomes

$$\frac{d^2\sigma_{\alpha\beta}}{d\Omega dE_x} = \sum_{E^*_b,E^*_B} \frac{m_\alpha m_\beta}{(2\pi\hbar^2)^2}\frac{k_\beta}{k_\alpha}\frac{1}{(2J_a+1)(2J_A+1)} \sum_{LM,J_1J_2} \left| \int d^3p N_{\alpha\beta}(\mathbf{k}_\alpha, \mathbf{k}_\beta, \mathbf{p}) Y_{LM}(\hat{\mathbf{p}}) M^{(J_aJ_A,J_bJ_B)}_{LJ_1J_2}(p^2)\right|^2 \delta(E^*_b + E^*_B - E_x). \tag{23}$$

The Dirac $\delta$ function projects the sum of excitation energies onto the total effective energy loss $E_x$.

The mathematical structure of the SCE amplitudes are strongly simplified for $J_a = 0^+ = J_A$. In that case, $J_1 = J_b$ and $J_2 = J_B$ and one obtains for the target [see Eq. (A13)]

$$F^{(AB)}_{\rm ST}(\mathbf{p}) = \sum_{L,M} (LMSM_S|J_BM_B) f^{(AB)}_{LSJ_B}(p^2) i^L Y_{LM}(\hat{\mathbf{p}}). \tag{24}$$

The same kind of relation holds for the projectile. Besides the triangle rule of angular momentum coupling, the allowed values of the orbital angular momentum transfer $L$ are constrained further by parity selection rules. For $0^+ \to J^{\pi_J}$ transitions $\pi_J = (-)^J$ and $\pi_J = (-)^{J+1}$ for natural and unnatural parity transitions, respectively, and $\pi_J = (-)^L$ must be fulfilled. For natural parity transitions with $L = J$, non-spin-flip $S = 0$ and spin-flip $S = 1$ transitions are allowed, while for unnatural parity transitions with $L = |J \pm 1|$ only transitions with $S = 1$ will contribute.

### B. Cross sections at low-momentum transfer

In the limit of low momentum transfer $\mathbf{q}_{\alpha\beta} = \mathbf{k}_\alpha - \mathbf{k}_\beta \to 0$, the distortion coefficient, Eq. (18), approaches in leading order a rather simple form:

$$N_{\alpha\beta}(\mathbf{k}_\alpha, \mathbf{k}_\beta, \mathbf{p}) \simeq \bar{N}_{\alpha\beta}(\mathbf{k}_\alpha, \mathbf{k}_\beta)\delta(\mathbf{p} - \mathbf{q}_{\alpha\beta}). \tag{25}$$

Hence, the momentum integration in Eq. (23) can be performed, by which the integrand is projected to $p = q_{\alpha\beta} \to 0$. The validity of this reduction will be discussed in detail below. The important point is that to a good approximation nuclear dynamics and reaction dynamics are becoming factorized in forward angle cross sections. Thus, once $\bar{N}_{\alpha\beta}$ has been determined, nuclear transition probabilities are becoming accessible. They are contained in the form factors $F^{(XY)}_{\rm ST}$ of Eq. (A13). More specifically, we need to consider the reduced form factors $f^{(XY)}_{LSJ}$ [see Eqs. (A13) and (A14)]. For small momenta $p \to 0$, we find

$$f^{(XY)}_{LSJ}(p^2) \sim \frac{p^L}{(2L+1)!!}\left[\int_0^\infty dr r^{2+L}\rho^{(XY)}_{LSJ}(r) + \mathcal{O}(p^2)\right], \tag{26}$$

given in leading order by the matrix element

$$b^{(XY)}_{LSJ} = \int_0^\infty dr r^{2+L}\rho^{(XY)}_{LSJ}(r), \tag{27}$$

which is the reduced transition amplitude of the multipole operator

$$\mathcal{B}_{(LST)JM}(\mathbf{r}) = r^L[Y_L \otimes (\boldsymbol{\sigma})^S]_{JM}(\boldsymbol{\tau})^T, \tag{28}$$

carrying the same functional structure as the $\beta$-decay transition operators. The corresponding excitation probability is given by

$$B^{(XY)}_{LSJ} = \frac{1}{2J+1}|\langle J_Y||\mathcal{B}_{LSTJ}||J_X\rangle|^2 = \left|b^{(XY)}_{LSJ}\right|^2. \tag{29}$$

Considering specifically transitions when both ions are in $0^+$ ground states, there will be for $J > 0$ in general two contributing multipole form factors, namely those of the $S = 0, 1$ transitions of the same $L = J$ for natural parity and those of the $L = J \pm 1$ transitions with fixed $S = 1$ for unnatural parity. For natural parity transitions, the superposition will

not modify the low-momentum behavior of the cross sections but has to be taken into account for the extraction of the corresponding transition strengths. At forward angles, the cross section for *natural parity* transitions in both nuclei will be of the type

$$\frac{d\sigma^{FF}}{d\Omega} \sim \frac{q^{2(J_a+J_A)}}{[(2J_a+1)!!(2J_A+1)!!]^2}|\bar{N}_{\alpha\beta}|^2 \times \left|V_{01}^{(C)}(0)b_{J_A0J_A}^{(AB)}b_{J_a0J_a}^{(ab)} + e^{i\phi_{aA}}V_{11}^{(C)}(0)b_{J_A1J_A}^{(AB)}b_{J_A1J_A}^{(AB)}\right|^2, \tag{30}$$

where $q = |k_\alpha - k_\beta|$ denotes the momentum transfer at forward direction and $\phi_{aA}$ accounts for possible relative phase factors of the target and projectile matrix elements. If one of the nuclei undergoes a $J = 0^+$ monopole excitation, i.e., a $0^+_{g.s.} \to 0^+_{E_x}$ transition, the $S = 1$ components will not contribute and irrespective of the multipolarity of the excitations in the second nucleus; only $S = 0$ transitions will be observed.

For unnatural parity states, the multipole mixtures lead to a modification of the momentum dependence because for $J \neq 0^-$ we have two angular momentum transfers, $L = J - 1$ and $L = J + 1$. The forward cross section for *unnatural parity* transitions in both nuclei behaves as

$$\frac{d\sigma^{GG}}{d\Omega} \sim \frac{q^{2(J_a+J_A-2)}}{[(2J_a-1)!!(2J_A-1)!!]^2}\left|V_{11}^{(C)}(0)\right|^2|\bar{N}_{\alpha\beta}|^2 \times \left[\left|b_{J_A-11J_A}^{(AB)} + \frac{q^2}{(2J_A+1)(2J_A+3)}b_{J_A+11J_A}^{(AB)}\right|^2 \times \left|b_{J_a+11J_a}^{(ab)} + \frac{q^2}{(2J_a+1)(2J_a+3)}b_{J_a+11J_a}^{(ab)}\right|^2\right]. \tag{31}$$

The contributions from the rank-2 tensor interactions are not shown because they will be suppressed at small momentum transfer. The multipole mixtures will change with the effective momentum transfer at forward directions. If there is a $0^-$ transition in one of the two nuclei, the corresponding transition form factor reduces to a single contribution with $L = 1$ and $S = 1$.

In addition, there are mixed transitions, combining a natural parity spin-flip excitation in one nucleus with unnatural excitations in the other nucleus. The corresponding cross sections are obtained in a similar way and are easily deduced by an appropriate combination of the above results.

## IV. INITIAL- AND FINAL-STATE INTERACTIONS

### A. Distorted waves and distortion coefficient

For heavy-ion reactions, the elastic interactions in the initial and the final channels play a key role for a quantitative description of cross sections. In a microscopic description, the optical potentials are obtained in a double-folding approach [17]. In the many cases where elastic scattering data are not available, the folding approach is in fact the only way to obtain information on elastic ion-ion interactions. The double-folding potential is defined in terms of the $NN$ $T$ matrix and the ground-state densities of the interacting nuclei. Thus, specific contributions, e.g., due to the coupling to breakup and transfer channels or rotational and vibrational excitations, are not included. Experience, however, shows that at kinetic energies above the Coulomb barrier the double-folding potential accounts surprisingly well for the elastic interactions over large ranges of incident energies and projectile-target combinations; see, e.g., Ref. [21]. The reason is that most of the interaction effects are already covered by the multiple scattering series inherent to an elastic amplitude iterated to all orders, as in the case of the solutions of a Schrödinger-type wave equation. A commonly used approach is the impulse approximation, amounting to consider the isoscalar and isovector ($S = 0, T = 0, 1$) parts of the free space $NN$ $T$ matrix. Since there are no heavy-ion polarization data available, spin-dependent parts of the optical potential are neglected. Coulomb interactions, of course, must be included as well. They are treated by folding the two-body projectile-target nucleon Coulomb interaction with the nuclear charge densities. Thus, we use

$$U_{\rm opt}(\mathbf{r}) = V(\mathbf{r}) - iW(\mathbf{r}) + U_c(\mathbf{r}), \tag{32}$$

where the imaginary part must in total correspond to an absorptive potential, guaranteeing a positive absorption cross section. The distorted waves are then defined by wave equations with the generic structure

$$\left(-\frac{\hbar^2}{2m_\gamma}\nabla^2 + U_\gamma(\mathbf{r}) - E_\gamma^{(\rm rel)}\right)\chi_\gamma^{(\pm)}(\mathbf{r}, \pm\mathbf{k}) = 0 \tag{33}$$

for $\gamma \in \{\alpha, \beta\}$. $E_{\alpha,\beta}^{\rm rel} = \sqrt{s} - M_{A,B} - M_{a,b}$ indicates the kinetic energy available in the projectile-target rest frame, with $M_{A,B}$ and $M_{a,b}$ denoting target and projectile rest masses.

### B. Separation approach to the distortion coefficient

From Eq. (18), the limiting case of a system without ISI and FSI interactions is immediately found by replacing the distorted waves by plane waves (PW). Then, the distortion coefficient reduces to

$$N_{\alpha\beta}^{(PW)}(\mathbf{k}_\alpha, \mathbf{k}_\beta, \mathbf{p}) = \delta(\mathbf{k}_\alpha - \mathbf{k}_\beta - \mathbf{p}) \tag{34}$$

and we retrieve the reaction amplitude, Eq. (19), in lowest-order Born approximation as

$$M_{\alpha\beta}^{(B)}(\mathbf{k}_\alpha, \mathbf{k}_\beta) \equiv \mathcal{U}_{\alpha\beta}(\mathbf{q}_{\alpha\beta}). \tag{35}$$

In order to establish the connection of the full distorted wave (DW) amplitudes to those of the PW limit, we need to consider the distortion coefficient in more detail. For that purpose, we separate the distorted waves $|\chi_{\alpha,\beta}^{(\pm)}\rangle$ into plane waves $|\mathbf{k}_{\alpha,\beta}\rangle$ and a residual distortion amplitude $u_{\alpha,\beta}^{(\pm)}(\mathbf{k}_{\alpha,\beta}, \mathbf{r})$. On very general grounds, such a separation is justified by the representation of an interacting wave in terms of the Møller-wave operator acting on a plane wave [22]. Assuming that $u_{\alpha,\beta}^{(\pm)}$ and $\mathcal{U}_{\alpha\beta}$ commute, we define the distortion density

$$\eta_{\alpha\beta} = u_\beta^{(-)\dagger}u_\alpha^{(+)}. \tag{36}$$

Then, Eq. (18) is found to be given by the Fourier transform of the distortion density

$$N_{\alpha\beta}(\mathbf{k}_\alpha, \mathbf{k}_\beta, \mathbf{p}) = \eta_{\alpha\beta}(\mathbf{q}_{\alpha\beta} - \mathbf{p}). \tag{37}$$

Since for a noninteracting system $\eta_{\alpha\beta}(\mathbf{r}) \to \eta^{(PW)}_{\alpha\beta}(\mathbf{r}) = 1$, it is useful to consider $\Delta_{\alpha\beta}(\mathbf{r}) = 1 - \eta_{\alpha\beta}(\mathbf{r})$. This allows to split the distortion coefficient as follows:

$$N_{\alpha\beta}(\mathbf{k}_\alpha, \mathbf{k}_\beta, \mathbf{p}) = N^{(PW)}_{\alpha\beta}(\mathbf{k}_\alpha, \mathbf{k}_\beta, \mathbf{p}) - \Delta_{\alpha\beta}(\mathbf{q}_{\alpha\beta} - \mathbf{p}), \quad (38)$$

where now the ISI and FSI effects are fully contained in the Fourier transform of $\Delta_{\alpha\beta}$. Correspondingly, the reaction amplitude divides into

$$\begin{aligned} M_{\alpha\beta}(\mathbf{k}_\alpha, \mathbf{k}_\beta) &= M^{(B)}_{\alpha\beta}(\mathbf{q}_{\alpha\beta}) - \int d^3p \Delta_{\alpha\beta}(\mathbf{q}_{\alpha\beta} - \mathbf{p}) M^{(B)}_{\alpha\beta}(\mathbf{p}) \\ &= M^{(B)}_{\alpha\beta}(\mathbf{q}_{\alpha\beta}) - \int d^3q \Delta_{\alpha\beta}(\mathbf{q}) M^{(B)}_{\alpha\beta}(\mathbf{q}_{\alpha\beta} - \mathbf{q}). \end{aligned} \quad (39)$$

Assuming that $\Delta_{\alpha\beta}$ is spherical symmetric, we obtain

$$\begin{aligned} &M_{\alpha\beta}(\mathbf{k}_\alpha, \mathbf{k}_\beta) \\ &\quad = M^{(B)}_{\alpha\beta}(\mathbf{q}_{\alpha\beta}) - 4\pi \int_0^\infty dq q^2 \Delta_{\alpha\beta}(q) \bar{M}^{(B)}_{\alpha\beta}(\mathbf{q}_{\alpha\beta}, q), \end{aligned} \quad (40)$$

where

$$\bar{M}^{(B)}_{\alpha\beta}(\mathbf{q}_{\alpha\beta}, q) = \frac{1}{4\pi} \int d\Omega_q M^{(B)}_{\alpha\beta}(\mathbf{q}_{\alpha\beta} - \mathbf{q}) \quad (41)$$

denotes the Born amplitude averaged over the orientations of $\mathbf{q}$. Referring to the definition of the Born amplitude, Eq. (35), the angle integral can be performed analytically, and we obtain

$$\bar{M}^{(B)}_{\alpha\beta}(\mathbf{q}_{\alpha\beta}, q) = \int d^3r e^{i\mathbf{q}_{\alpha\beta}\cdot\mathbf{r}} \mathcal{U}_{\alpha\beta}(\mathbf{r}) j_0(qr). \quad (42)$$

The above relations involve in fact different scales, which allow a separation ansatz: The distribution of the momenta $q$ is controlled by the optical model quantity $\Delta_{\alpha\beta}$ with a typical momentum spread of the order of the potential radius, i.e., $\Delta q_{\text{reac}} \sim \frac{1}{R_{\text{opt}}} \leqslant 50$ MeV/c. The momentum structure of the Born amplitude is determined by the charge-changing nuclear form factors $F^{(ab),(AB)}$. Their overall momentum dependence is closely related to the Fermi momenta of protons and neutrons; thus $\Delta q_{\text{nucl}} \sim k_F \sim 300$ MeV/c. Therefore, we introduce the separation ansatz

$$\bar{M}^{(B)}_{\alpha\beta}(\mathbf{q}_{\alpha\beta}, q) \simeq M^{(B)}_{\alpha\beta}(\mathbf{q}_{\alpha\beta}) h_{\alpha\beta}(q), \quad (43)$$

where the separation function $h_{\alpha\beta}(q)$ is determined by the variation of the Born amplitude off the physical 3-momentum shell $\mathbf{q}_{\alpha\beta}$.

Now, we perform the remaining integral and define the absorption index

$$n_{\alpha\beta} = 4\pi \int_0^\infty dq q^2 \Delta_{\alpha\beta}(q) h_{\alpha\beta}(q). \quad (44)$$

The full reaction amplitude acquires a considerably simplified structure,

$$M_{\alpha\beta}(\mathbf{k}_\alpha, \mathbf{k}_\beta) = M^{(B)}_{\alpha\beta}(\mathbf{q}_{\alpha\beta})(1 - n_{\alpha\beta}), \quad (45)$$

given in leading order by the Born amplitude, scaled by a distortion coefficient which should depend only weakly on the momentum transfer for a meaningful factorization of $M_{\alpha\beta}$.

### C. Separation function for Gaussian form factors

The separation ansatz discussed above can be checked, on an analytical basis, if one adopts a Gaussian shape, $U_G$, for the transition potential $\mathcal{U}_{\alpha\beta}(\mathbf{p})$. Indeed, nuclear SCE transitions are well modeled by surface form factors for which the Gaussian shape is a quite convenient and realistic choice. For the present purpose, it is sufficient to consider a transition potential with a single Gaussian form factor,

$$\mathcal{U}_G(\mathbf{r}, \mathbf{R}) = \frac{1}{4\pi} U_0 e^{-\frac{(\mathbf{r}-\mathbf{R})^2}{2\sigma^2}}, \quad (46)$$

which can be adjusted to microscopically derived shapes by an appropriate choice of the centroid parameter $R$ and the width parameter $\sigma$. Considered as classical quantities, $R$ and $\sigma$ are determined, in principle, by the radii and surface thicknesses of the colliding ions. $\mathcal{U}_G$ contains a rich multipole structure

$$\mathcal{U}_G(\mathbf{r}, \mathbf{R}) = \sum_{LM} Y^*_{LM}(\hat{\mathbf{R}}) U_{LM}(\mathbf{r}, R) \quad (47)$$

with the multipole form factors

$$U_{LM}(\mathbf{r}, R) = \int d\hat{R} Y_{LM}(\hat{\mathbf{R}}) U_G(\mathbf{r}, \mathbf{R}) \quad (48)$$

$$= U_0 e^{-\frac{r^2+R^2}{2\sigma^2}} i_L(rR/\sigma^2) Y_{LM}(\hat{\mathbf{r}}), \quad (49)$$

where $i_L(x) = i^L j_L(ix)$ is a modified spherical Bessel function. As discussed in Appendix C, the connection to the microscopic structure of the intrinsic nuclear transitions involved in projectile and target is recovered by imposing on $Y_{LM}(\hat{\mathbf{R}})$ a quantization condition in terms of the projectile and target state operators, similar to the collective model of nuclear excitations. There, it is also shown that within the Gaussian approximation $R$ and $\sigma$ are determined by the corresponding projectile and target quantities. The strength parameter $U_0$ is related to the volume integral of the $NN$ $T$ matrix. However, for the following those details are of minor relevance because state-independent, universal properties of distortion effects in nonelastic ion-ion reactions are investigated. Thus, for simplicity, we neglect the state dependence, choose $U_0 = 1$, and leave the determination of $R$ and $\sigma$ for later.

The Fourier-Bessel transform is derived analytically,

$$\mathcal{U}_G(\mathbf{p}, \mathbf{R}) = \sqrt{\frac{\pi}{2}} \sigma^3 e^{i\mathbf{p}\cdot\mathbf{R}} e^{-\frac{1}{2}\sigma^2 p^2}, \quad (50)$$

and the momentum space multipoles are obtained as above by projecting on $Y_{LM}(\hat{\mathbf{R}})$. This amounts to expand the plane wave into partial waves, resulting in

$$U_{LM}(\mathbf{p}, R) = 4\pi \sqrt{\frac{\pi}{2}} \sigma^3 e^{-\frac{1}{2}\sigma^2 p^2} j_L(pR) i^L Y_{LM}(\hat{\mathbf{p}}). \quad (51)$$

According to Eq. (39), we need to evaluate $U_G(\mathbf{p})$ at $\mathbf{p} = \mathbf{q}_{\alpha\beta} - \mathbf{q}$. This leads to

$$\mathcal{U}_G(\mathbf{q}_{\alpha\beta} - \mathbf{q}, \mathbf{R}) = \mathcal{U}_G(\mathbf{q}_{\alpha\beta}, \mathbf{R}) \mathcal{H}_{\alpha\beta}(\mathbf{q}, \boldsymbol{\rho}), \quad (52)$$

describing the (partial) separation of the dependencies on the physical momentum transfer $\mathbf{q}_{\alpha\beta}$ and the momentum shift $\mathbf{q}$ due to the ISI-FSI interactions by means of

$$\mathcal{H}_{\alpha\beta}(\mathbf{q}, \boldsymbol{\rho}) = e^{-\frac{1}{2}\sigma^2 q^2} e^{-i\mathbf{q}\cdot\boldsymbol{\rho}} \quad (53)$$

with the pseudoradius

$$\boldsymbol{\rho} = \mathbf{R} + i\sigma^2 \mathbf{q}_{\alpha\beta}, \tag{54}$$

which is shifted into the complex plane by an amount controlled by the width parameter $\sigma$. We use $\rho = \sqrt{\rho^2}$, where

$$\rho^2 = R^2 - \sigma^4 q_{\alpha\beta}^2 + 2i\sigma^2 \mathbf{q}_{\alpha\beta} \cdot \mathbf{R}. \tag{55}$$

Since $\rho$ also depends on the on-shell momentum transfer $\mathbf{q}_{\alpha\beta}$, the separation of variables is not yet fully achieved. The function $h_{\alpha\beta}$ of Eq. (43) is given as

$$h_{\alpha\beta}(q,\rho) = \frac{1}{4\pi} \int d\hat{\mathbf{q}} \mathcal{H}_{\alpha\beta}(\mathbf{q},\boldsymbol{\rho}) = e^{-\frac{1}{2}\sigma^2 q^2} j_0(q\rho) \tag{56}$$

and the distortion coefficient $(1 - n_{\alpha\beta})$ is found according to Eq. (44). Further insight into the modification introduced by the ion-ion ISI and FSI interactions is obtained by using the addition theorem for Bessel functions [23]

$$j_0(q\rho) = \sum_\lambda (2\lambda+1) P_\lambda(\cos\gamma) j_\lambda(qR) i^\lambda i_\lambda(q q_{\alpha\beta}\sigma^2), \tag{57}$$

where $\gamma$ denotes the angle between $\mathbf{R}$ and $\mathbf{q}_{\alpha\beta}$. Furthermore, using the addition theorem of spherical harmonics, we find

$$h_{\alpha\beta}(q,\rho) = 4\pi e^{-\frac{1}{2}\sigma^2 q^2} \sum_{\lambda\mu} i^\lambda Y_{\lambda\mu}(\hat{\mathbf{q}}_{\alpha\beta}) Y^*_{\lambda\mu}(\hat{\mathbf{R}}) j_\lambda(qR) i_\lambda(q q_{\alpha\beta}\sigma^2). \tag{58}$$

For momentum transfers in the range $q_{\alpha\beta} \ll 1/\sigma$, which amounts to about the order of 100 MeV/c, the sum is well approximated by the monopole term,

$$h_{\alpha\beta}(q) = e^{-\frac{1}{2}\sigma^2 q^2} j_0(qR) i_0(q q_{\alpha\beta}\sigma^2), \tag{59}$$

indicating a remaining dependence on the reaction momentum transfer. This derivation, based on the Gaussian form factor, allows one to understand the range of validity of the separation ansatz, Eq. (43). Indeed, for transferred momenta approaching zero, one recovers the complete factorization discussed above, i.e.,

$$h_{\alpha\beta}(q) \mapsto e^{-\frac{1}{2}\sigma^2 q^2} j_0(qR). \tag{60}$$

## V. DISTORTION COEFFICIENT IN THE STRONG ABSORPTION LIMIT

### A. Strong absorption limit and black disk approximation

In the derivation of Eq. (45), the critical step is clearly the treatment of the distortion effects, which we consider next. For strongly absorbing systems like ion-ion scattering, the distorted waves are almost completely suppressed in the overlap region, thus reflecting the large amount of channel coupling which leads to a redirection of the incoming elastic probability flux into a multitude of nonelastic reaction channels. Such systems are described by optical potentials with a strong imaginary part of a strength comparable in magnitude to the real, diffractive part. Under such conditions, the distortion amplitude introduced before resembles in coordinate space a step function, $\eta_{\alpha\beta}(\mathbf{r}) \sim e^{i\phi(\mathbf{r})}\Theta(r - R_{\rm abs})$. In the following, we neglect the phase factor given by $\phi$. This picture coincides with the *black disk assumption* (BD), where one considers that a major part of the incoming flux is consumed by a (spherical) absorber of radius $R_{\rm abs}$, resulting in the total absorption cross section

$$\sigma_{\rm abs}^{\rm (BD)}(\sqrt{s}) = \pi R_{\rm abs}^2(\sqrt{s}), \tag{61}$$

and by equating $\sigma_{\rm abs}^{\rm (BD)}$ and the quantum mechanical reaction cross sections $\sigma_{\rm abs}^{(\alpha,\beta)}$ the absorption radius $R_{\rm abs}$ is obtained. Considering that $\sigma_{\rm abs} \sim 1$–$3$ b as a representative range of values for ion-ion reaction cross sections at energies of a few 10 A MeV we find $R_{\rm abs} \sim 5$–$10$ fm. These values are implying a variation of the function $j_0(qR_{\rm abs})$ on a momentum scale $\Delta q_{\rm reac} \sim 1/R_{\rm abs} \sim 20$–$40$ MeV/c, thus complying perfectly well with the previous estimates.

In the BD limit, we can evaluate the distortion coefficient in closed form. We find

$$\Delta_{\alpha\beta}^{\rm (BD)}(q) = \frac{1}{2\pi^2} \frac{R_{\rm abs}}{q} \left(-\frac{\partial}{\partial q}\right) j_0(qR_{\rm abs}) \tag{62}$$

and the scaling function is given by

$$n_{\alpha\beta}^{\rm (BD)}(R_{\rm abs}) = \frac{2R_{\rm abs}}{\pi} \int_0^\infty dq j_0(qR_{\rm abs}) \frac{\partial}{\partial q}[q h_{\alpha\beta}(q)], \tag{63}$$

which corresponds to a Fourier-Bessel transform of $h_{\alpha\beta}(q)$, mapping the dependence on the variable $q$ to the complementary variable $R_{\rm abs}$. As discussed in Appendix D, for $h(q)$ given by Eq. (56), the black disk distortion coefficient can be calculated in closed form, resulting in a superposition of error integrals and Gaussians.

In $h_{\alpha\beta}$, see Eq. (56), the parameter $\sigma$ controls the slope of the momentum distribution around the physical momentum transfer $q_{\alpha\beta}$. By the arguments given above, we expect $\sigma \sim \mathcal{O}(1/k_F)$, thus being related to the binding properties of nuclei. Hence, the width of the Gaussian form factor is determined by the surface diffuseness of nuclear density distributions. The (off-shell) diffraction structure of the transition form factors, which is described by $R$, is more directly affected by the nuclear geometry, which to a large extent is a mean-field effect, thus related to the radii of the nuclear densities, $R_{a,A}$. Taking into account the modifications by the folding with the $NN$ interaction, we estimate therefore $R \sim \mathcal{O}(R_{\rm pot})$, where $R_{\rm pot}$ is the radius of the ion-ion potential.

### B. Relation to eikonal theory

The distortion coefficient, Eq. (18), approaches a well-known limit for $\mathbf{p} \to 0$, given by the $S$ matrix [24]. Evaluating explicitly the case $\alpha = \beta$ gives

$$N_{\alpha\beta}(\mathbf{k}_\alpha, \mathbf{k}_\beta, \mathbf{p})_{p=0} \to N_D = \frac{1}{(2\pi)^3} \langle \chi_\alpha^{(-)} | \chi_\alpha^{+} \rangle = \frac{1}{k_\alpha^2} \delta(k_\alpha - k'_\alpha) \frac{1}{4\pi} S_\alpha, \tag{64}$$

resulting in the optical model $S$ matrix, given by the partial-wave $S$-matrix elements $S_\ell$:

$$S_\alpha = \sum_\ell (2\ell+1) P_\ell(\cos\theta) S_\ell. \tag{65}$$

The $\delta$ function takes care of energy conservation, reflecting the on-shell property of the $S$ matrix. In the on-shell limit, the quantity $\Delta_{\alpha\beta}$, Eq. (38), is determined by the elastic scattering amplitude. Hence, the distortion coefficient can be understood as an off-shell extension of the elastic scattering amplitude.

Averaging the modulus squared of $S_\alpha$ over the final momentum direction, we find

$$\langle |S_\alpha|^2 \rangle = \sum_\ell (2\ell+1)|S_\ell|^2. \tag{66}$$

Removing the divergent part of that summation—reminiscent of the $\delta$ function deriving from the plane-wave components—we end up with the absorption coefficients $A_\ell = 1 - |S_\ell|^2$, which determine also the total reaction cross section. Thus, in the case of the strong absorption characterizing heavy-ion collisions, the distortion coefficient is closely related to the reaction cross section.

At incident energies well above the Coulomb barrier, eikonal theory is in fact a suitable method to investigate further distortion effects. The absorptive heavy-ion interactions allow us to use eikonal theory already at the relatively low energies as considered here. In the nuclear interior where also the real potential is sizable, the deep imaginary potential suppresses the scattering waves by many orders of magnitude. Thus, to a large extent the reaction is blind against the region where the potentials may be of the same magnitude or even larger than the kinetic ion-ion energy. The scattering process is determined by the regions where the imaginary potential strength has decreased to values smaller than the real part of the potential plus the kinetic energy.

In eikonal theory, the $S$ matrix is given by an integral over impact parameters $b$

$$S_\alpha = \frac{1}{2\pi}\int_0^\infty dbbJ_0(qb)e^{i\chi_\alpha(\mathbf{b})}, \tag{67}$$

where $J_0(x)$ is the ordinary Bessel function of order $n = 0$, $q = |\mathbf{k}_\alpha - \mathbf{k}'_\alpha|$ denotes the elastic momentum transfer. The $S$ matrix is given now by the profile function $\chi_\alpha(\mathbf{b})$ depending on the impact parameter $b$, as discussed in Appendix E. A projection on vanishing longitudinal momentum transfer $q_z = 0$ is obtained reflecting the fact that distortion affects in the first place the transversal components of scattering wave functions. Thus, finally we obtain[1]

$$\langle |S_\alpha|^2 \rangle = \frac{1}{2\pi}\int_0^\infty dbbe^{-2Im(\chi_\alpha(b))}. \tag{68}$$

In Fig. 2, the quantum mechanical absorption factor $A_l = 1 - |S_\ell|^2$, evaluated numerically, and the eikonal analog $1 - |S(b)|^2$ are compared for the reaction $^{18}\mathrm{O} + ^{40}\mathrm{Ca}$ at $T_{\mathrm{Lab}} = 15$ A MeV. The same optical potential is used, assuring that the reaction cross section is reproduced in eikonal approximation (see next section). The agreement is striking. The reason that eikonal theory is doing so well at this low energy

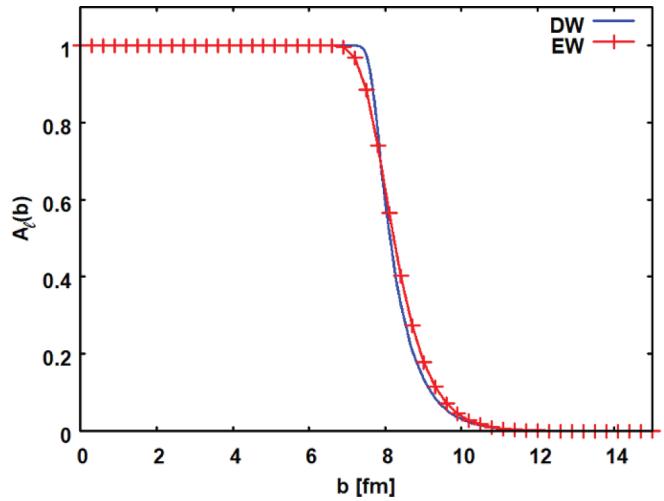


FIG. 2. Comparison of quantum mechanical (DW) and eikonal (EW) results for the absorption factors $A_\ell = 1 - |S_\ell|^2$ shown as functions of the impact parameter $b \simeq \ell/k_\alpha$.

is the strong absorption by which contributions of $\mathrm{Re}[\chi(b)]$ are strongly suppressed in the space regions where $\mathrm{Im}(U_{\mathrm{opt}})$ is sizable.

### C. Mass and energy dependence of absorption effects

An important conclusion from the foregoing discussion is the paramount role of absorption effects for which the absorption radius $R_{\mathrm{abs}}$ is the key quantity. Moreover, according to Appendix E, in the strong absorption limit the distortion coefficient is fixed once $R_{\mathrm{abs}}$ is known, together with the nuclear shape parameters. For our purpose, it is enough to consider the imaginary part of the optical potential $W(\mathbf{r})$. In the present context, $W(\mathbf{r})$ plays the role of an effective eikonal potential which has to be adjusted such that the quantal results are reproduced as close as possible. A spherical-symmetric potential of Gaussian shape is used:

$$W(r) = -W_0 e^{-r^2/R_W^2}. \tag{69}$$

The radius parameter $R_W$ and the potential strength are fixed by comparison to quantum mechanical results for the total reaction cross section for two reference systems: $^{18}\mathrm{O} + ^{40}\mathrm{Ca}$ and $^{18}\mathrm{O} + ^{116}\mathrm{Sn}$ at $T_{\mathrm{lab}} = 270$ MeV [13]. Denoting the mass numbers of projectile and target by $A_{p,T}$, a proper description of the two systems is obtained with $R_W = r_0\sqrt{A_p^{\frac{2}{3}} + A_T^{\frac{2}{3}}}$, where $r_0 = 0.783$ fm and

$$W_0 = w\left(A_p^{\frac{2}{3}} + A_T^{\frac{2}{3}}\right)^{-3/4}, \tag{70}$$

with $w = 5902.743$ MeV. Interestingly, the potential depth behaves according to the so-called $UR^\alpha$ law, which was found in the early days of the nuclear optical model by Hodgson [25,26], when studying ambiguities of optical potentials. In our case, we have $\alpha = 3/2$. We also note that the eikonal approximation works rather well for shallow optical potentials, as given by our parametrization. For instance, for the system $^{18}\mathrm{O} + ^{40}\mathrm{Ca}$ we find $R_W \simeq 3.375$ fm and strength $W_0 \simeq 660$ MeV, resulting in $\sigma_{\mathrm{abs}}^{(\alpha)} \simeq 2.14$ b and $R_{\mathrm{abs}} \simeq 8.26$ fm. As

[1]At low energies, Coulomb barrier effects may be taken into account by the additional factor $e^{-2\pi\eta_S}$, where $\eta_S$ is the Sommerfeld parameter.

discussed in Sec. IV C, the transition potential is described by a surface-centered Gaussian,

$$U_G(\mathbf{r}, \mathbf{R}_G) \sim e^{-(\mathbf{r}-\mathbf{R}_G)^2/2\sigma^2} \tag{71}$$

with $R_G = r_G\sqrt{A_P^{\frac{2}{3}} + A_T^{\frac{2}{3}}}$, $r_G = 1.2$ fm. The width parameter $\sigma \approx 1$ fm corresponds to the width obtained by folding two nuclear transition form factors of Gaussian shape, each with $\sigma_{a,A} \sim 0.7$ fm (see Appendix C and Sec. IV C).

Thus, we have at hand all quantities necessary to evaluate the distortion amplitude $\eta_{\alpha\beta}$ and the total absorption cross section $\sigma_{\rm abs}^{(\alpha,\beta)}$ as functions of mass and energy, by the formalism of Appendix E. Then, from the absorption radius, we derive, within the black disk approximation, the distortion coefficient $(1 - n_{\rm BD})$ and the distortion factor $f_{\rm BD} = |1 - n_{\rm BD}|^2$ (see Appendix D).

The dependence of $R_{\rm abs}(A_P, A_T, T_{\rm Lab})$ on the ion masses and the incident energy is illustrated in Fig. 3. The variation of the ratio $R_{\rm abs}/R_W$ on the target mass number $A_T$ is displayed on the upper panel for the three choices of projectiles, namely $^{12}$C, $^{18}$O, and $^{28}$Si at fixed energy $T_{\rm Lab} = 270$ MeV. The ratio decreases mildly by a few percent with increasing $A_T$, implying an $A^{1/3}$ dependence for $R_{\rm abs}$. A slight increase with $A_P$ is found, reflecting slightly larger variation with the projectile mass.

In the lower panel of Fig. 3, the dependence of $R_{\rm abs}/R_W$ on the incident energy is shown, fixing the target to $^{40}$Ca. Here, one finds a behavior similar to the mass dependence: The absorption radii decrease continuously with increasing incident energy. From Eqs. (E16) and (E17), one finds for small energies a logarithmically divergent dependence on $T_{\rm Lab}$, which for large energies changes to a dependence on $1/k_\alpha \sim 1/\sqrt{T_{\rm lab}}$.

The mass and energy dependences of the distortion factor $f_{\rm BD}$ are explored in Fig. 4. Over the shown mass range, a decrease by several orders of magnitude is found, indicating the smallness of cross sections to be expected for heavy targets and increasing projectile mass. The results indicate, on the other hand, that lighter projectiles are leading to a less extreme suppression.

As a function of energy, $f_{\rm BD}$ increase rapidly with $T_{\rm Lab}$ as seen in the lower panel of Fig. 4. Thus, combining these results with those on the mass dependence, we conclude that already a moderate increase of the incident energy will lead to considerably larger cross sections also for heavier target-projectile combinations.

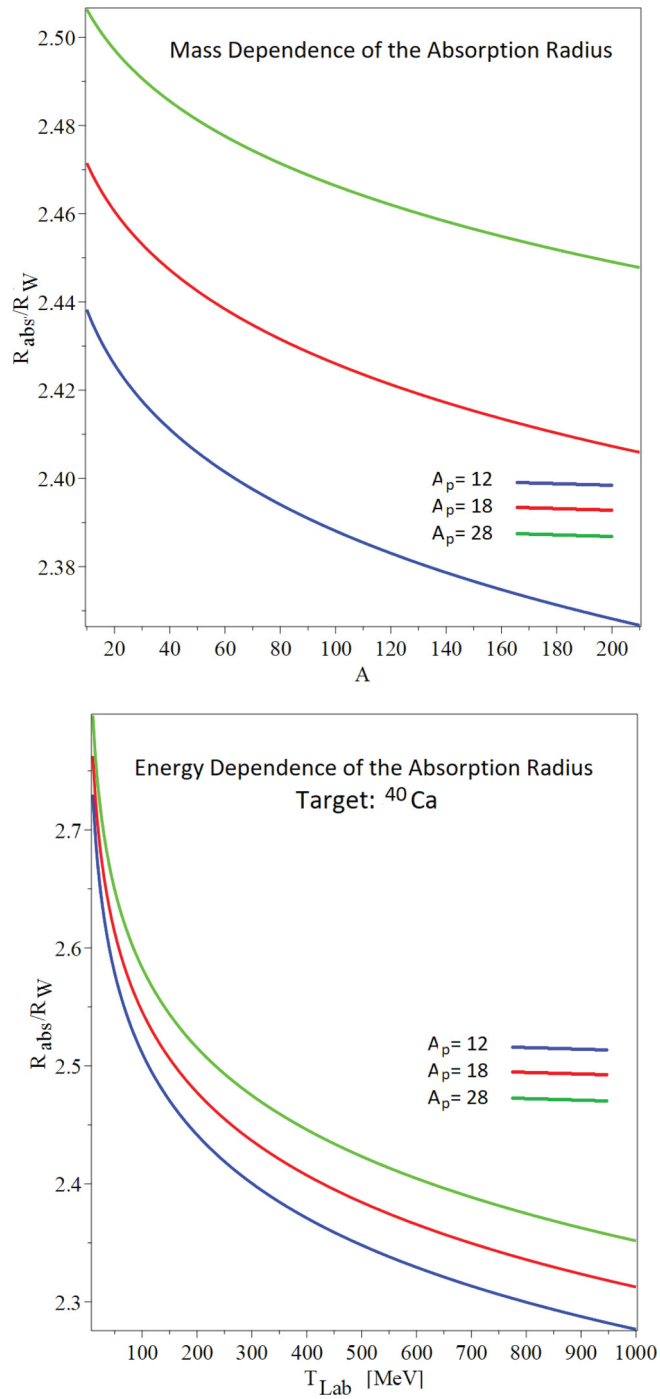


FIG. 3. Upper panel: Variation of the effective absorption radius $R_{\rm abs}$ with projectile and target mass. Gauss-eikonal-approximation (GEA) results are shown for the projectiles $^{12}$C (lower curve, red), $^{18}$O (center curve, red), and $^{28}$Si (upper curve, green), respectively, on targets with mass numbers $10 \leqslant A_T \leqslant 210$. Lower panel: Variation of the effective absorption radius $R_{\rm abs}$ with incident energy. GEA results are shown for reactions on $^{40}$Ca with the projectiles $^{12}$C (lower curve, red), $^{18}$O (center curve, red), and $^{28}$Si (upper curve, green), respectively.

## VI. APPLICATIONS TO HEAVY-ION-INDUCED SCE REACTIONS

### A. Spectroscopy of charge changing nuclear excitations

The theoretical methods developed in the previous sections are mainly applied in the following to the SCE reaction $^{18}\mathrm{O} + {}^{40}\mathrm{Ca} \rightarrow {}^{18}\mathrm{F} + {}^{40}\mathrm{K}$, at $T_{\rm lab} = 15$ A MeV [27], which has been recently investigated by the NUMEN Collaboration [12]. Some illustrative results will be also shown at different beam energies and for the $^{18}\mathrm{O} + {}^{116}\mathrm{Sn} \rightarrow {}^{18}\mathrm{F} + {}^{116}\mathrm{In}$ reaction. In this section, we consider first charge changing nuclear excitations in a self-consistent approach using nuclear HFB mean-field theory for ground states and QRPA theory for the transition densities. In combination, these two methods provide a versatile toolbox with appropriate instruments for

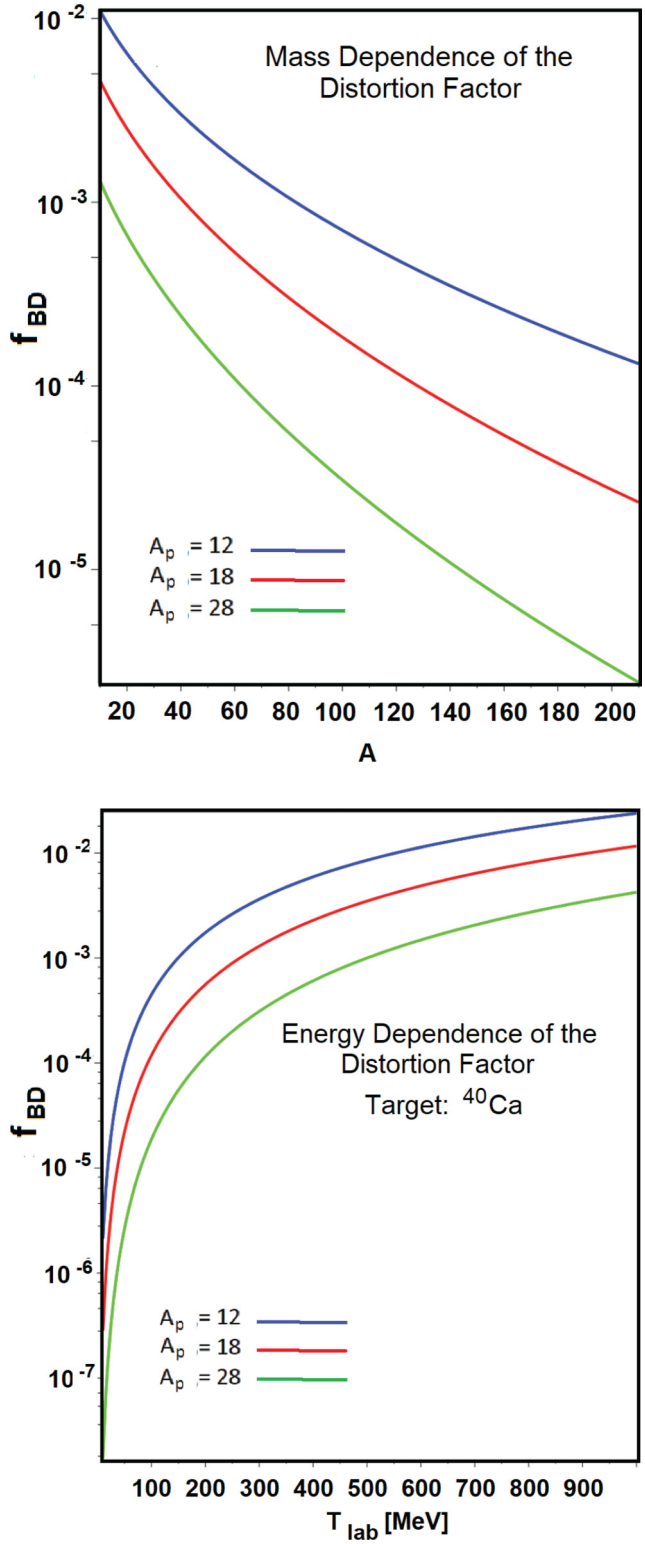


FIG. 4. Upper panel: Variation of the distortion factor $f_{\mathrm{BD}}$ with projectile and target mass. GEA results are shown for the projectiles $^{12}$C (lower curve, red), $^{18}$O (center curve, red), and $^{28}$Si (upper curve, green), respectively, on targets with mass numbers $10 \leqslant A_T \leqslant 210$. Lower panel: Variation of the distortion factor $f_{\mathrm{BD}}$ with incident energy. GEA results are shown for reactions on $^{40}$Ca with the projectiles $^{12}$C (upper curve, red), $^{18}$O (center curve, red), and $^{28}$Si (lower curve, green), respectively.

TABLE I. Ground-state properties of the $A = 18$ and the $A = 40$ isobars. The observed and the calculated binding energies per nucleon are shown in the second and third columns. Density and charge root-mean-square radii are noted by $r_d$ and $r_{\mathrm{chrg}}$, respectively. The data are taken from the AMDC mass evaluation [30].

| Nucleus | $B_{\mathrm{exp}}(A)/A$ [MeV/A] | $B_{\mathrm{theo}}(A)/A$ [MeV/A] | $r_d$ [fm] | $r_{\mathrm{chrg}}$ [fm] |
|---|---|---|---|---|
| $^{18}$N | 7.038 | 7.236 | 2.790 | 2.693 |
| $^{18}$O | 7.767 | 7.894 | 2.740 | 2.757 |
| $^{18}$F | 7.632 | 7.329 | 2.763 | 2.854 |
| $^{40}$K | 8.538 | 8.620 | 3.369 | 3.449 |
| $^{40}$Ca | 8.551 | 8.618 | 3.373 | 3.486 |
| $^{40}$Sc | 8.174 | 8.269 | 3.381 | 3.524 |

the proper description of nuclear spectroscopy over most of the nuclear mass table, except for the lightest nuclei. The reaction theoretical aspects will be addressed afterward. There, the focus will be in the first place to clarify and establish a couple of special aspects of heavy-ion reactions at intermediate energies, rather than fitting data.

#### *1. HFB mean-field description of the $A = 18$ and $A = 40$ isobars*

For the practical calculations, the quasiparticle spectrum and the single-particle wave functions are obtained by density functional theory. An energy density functional (EDF) along the line of Refs. [19,28] is constructed, using a $G$ matrix interaction, supplemented by three-body terms. First variation leads to single-particle-wave equations with effective density-dependent potentials and pairing interactions, solved self-consistently by HFB and BCS methods. In the particle-particle channel, an effective density-dependent contact pairing interaction is used. The strength is derived from the $nn$ and $pp$ singlet-even Born matrix elements of the Bonn interaction in the nonrelativistic reduction found in Ref. [29]. Such an approach leads to state-dependent pairing gaps which are determined self-consistently in parallel to the HFB iteration procedure. In Table I, HFB results for the ground states of mass-18 and mass-40 nuclei are listed. For the $A = 18$ isobars, the measured binding energies are reproduced by better than 4%. As typical for a mean-field description with global parameter sets, the agreement improves with increasing mass. The binding energies of the $A = 40$ isobars are described by better than about 1%. A similar dependence will also be detected for the QRPA results discussed below. For the single-particle spectra entering into the QRPA calculations, proton and neutron continuum states are included up to single-particle energies of 100 MeV. They are obtained by using the self-consistent HFB mean-field potentials, thus avoiding artificial, nonphysical nonorthogonality effects. The single-particle continua are described by a dense spectrum of discrete states. Enclosing the system into a spherical cavity of a size of up to 100 fm, an average energy spacing of about 20 keV is obtained. The optical potentials discussed above are calculated with the $^{18}$O and $^{40}$Ca HFB ground-state densities. They are displayed in Fig. 5.

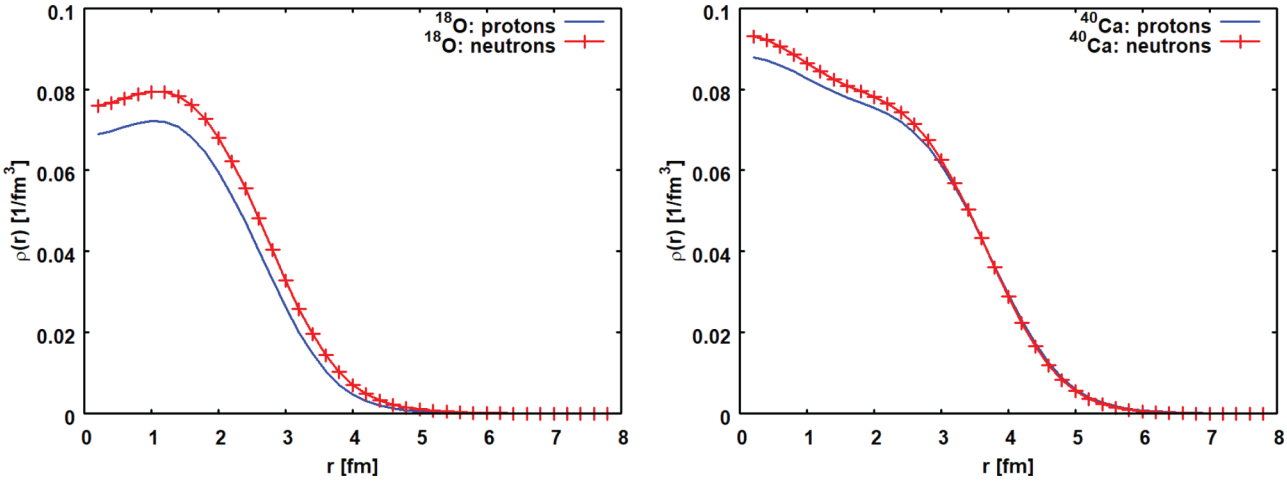


FIG. 5. Proton and neutron HFB ground-state densities for $^{18}$O (left) and $^{40}$Ca (right), respectively. In $^{18}$O, the onset of a neutron skin is visible.

### 2. SCE response functions

Nuclear charge changing excitations consist of two branches: The $np^{-1}$ branch probes the $\tau_+$ response and $pn^{-1}$ excitations probes the $\tau_-$ response, intimately related to the $\beta^{\pm}$ processes of weak interactions. In both $^{18}$O and $^{40}$Ca, however, the mixing of the two branches is negligible.

Physically, the 2QP configurations will be coupled to 4QP and higher order many-body configurations. These couplings induce non-Hermitian polarization self-energies $\Sigma_{QQ}(\omega) = \Delta_c(\omega) - \frac{i}{2}\Gamma_c(\omega)$ where real and imaginary parts are connected by a dispersion relation. The self-energies are described by a global energy-dependent parametrization according to the procedure discussed in Refs. [31,32].

The residual interactions are obtained by second variation of the same EDF as used in the HFB ground-state calculations, leading to density-dependent Landau-Migdal parameters. For the present purpose, the isovector interactions are of primary interest. Because of the density dependence, the Landau-Migdal interactions include rearrangement contributions describing an additional effective screening of the 2QP interaction vertices and wave function renormalizations.

Below, results of our nuclear structure calculations will be discussed for charge-changing excitations of $^{18}$O and $^{40}$Ca. As test operators, we use the multipole operators

$$T_{\mathrm{LSJM}} = \left(\frac{r}{R_d}\right)^L [\boldsymbol{\sigma}^S \otimes Y_L]_{JM}\tau_{\pm}, \tag{72}$$

which are of a structure similar to the weak interaction operators of nuclear $\beta$ decay. However, here we consider the full spectrum of spatial and spin multipoles; i.e., we also include response functions for transitions which would be strongly suppressed in $\beta$ decay. The normalization to the half-density radius $R_d$ of the respective parent nucleus removes to a large extent the (trivial) dependence of response functions on the nuclear size. In the following, all data on energy spectra were taken from the NNDC online compilation [33].

### 3. Charge-changing response functions for $^{18}$O

The HFB ground state of $^{18}$O is given by a semimagic configuration: For the protons, the perfect $Z = 8$ shell closure as in $^{16}$O is maintained but the two valence neutrons are in an open-shell configuration in the $d_{\frac{5}{2}}$ shell. Thus, the two charge-exchange branches involve quite different configurations. The low-energy $np^{-1}$ excitations lead to negative-parity $J^P = 0^-, 1^-, 2^-, 3^-$ ground-state multiplet of states in $^{18}$N, as allowed by the transitions from the $1p$-proton shell to the $(2s, 1d)$-neutron shell. Experimentally, one finds $^{18}N(1^-, \text{g.s.})$, followed by states at $E_x = 115$ keV and $E_x = 588$ keV, tentatively assigned as $J^P = 2^-$, and a tentative $J^P = 3^-$ state at $E_x = 747$ keV but the $J^P = 0^-$ state is missing. The low-energy spectrum of the complementary $pn^{-1}$ branch, populating states in $^{18}$F, is determined by configuration of $1d_{\frac{5}{2}}$ neutron hole states and proton states in the $(2s, 1d)$ shell. In principle, this allows a ground-state sextet with $J^P = 0^+, 1^+, 2^+, 3^+, 4^+, 5^+$. Experimentally, a $^{18}\mathrm{F}(1^+, \text{g.s.})$ is found, followed by a $J^P = 3^+$ state at $E_x = 937$ keV, a $J^P = 0^+$ state at $E_x = 1042$ keV, and a $J^P = 5^+$ state at $E_x = 1121$ keV. The first $J^P = 2^+$ state is found at the much higher energy $E_x = 2523$ keV. Thus, a much richer spectrum than in $^{18}$N is observed. At $E_x = 1181$ keV, a $J^P = 0^-$ is observed and at $E_x = 2101$ keV a $J^P = 2^-$ state is seen. These negative- parity intruder states indicate an imperfect closure of the proton $1p$ shell.

In contrast to the data, the QRPA calculations lead to a somewhat more spread out spectrum. Overall, however, the agreement is very satisfactory in view of the restriction to the 2QP-configuration space. The model calculations, shown in Fig. 6, predict a $J^P = 4^+$ ground state, followed by a $J^P = 5^+$ state at $E_x = 172$ keV, a nearby $J^P = 3^+$ state at $E_x = 197$ keV, and a $J^P = 2^+$ state at $E_x = 305$ keV. Another $J^P = 2^+$ state is obtained at $E_x = 980$ keV. At $E_x = 3298$ keV and $E_x = 4049$ keV, a $J^P = 0^+$ doublet is predicted. The two states may be the theoretical counterparts

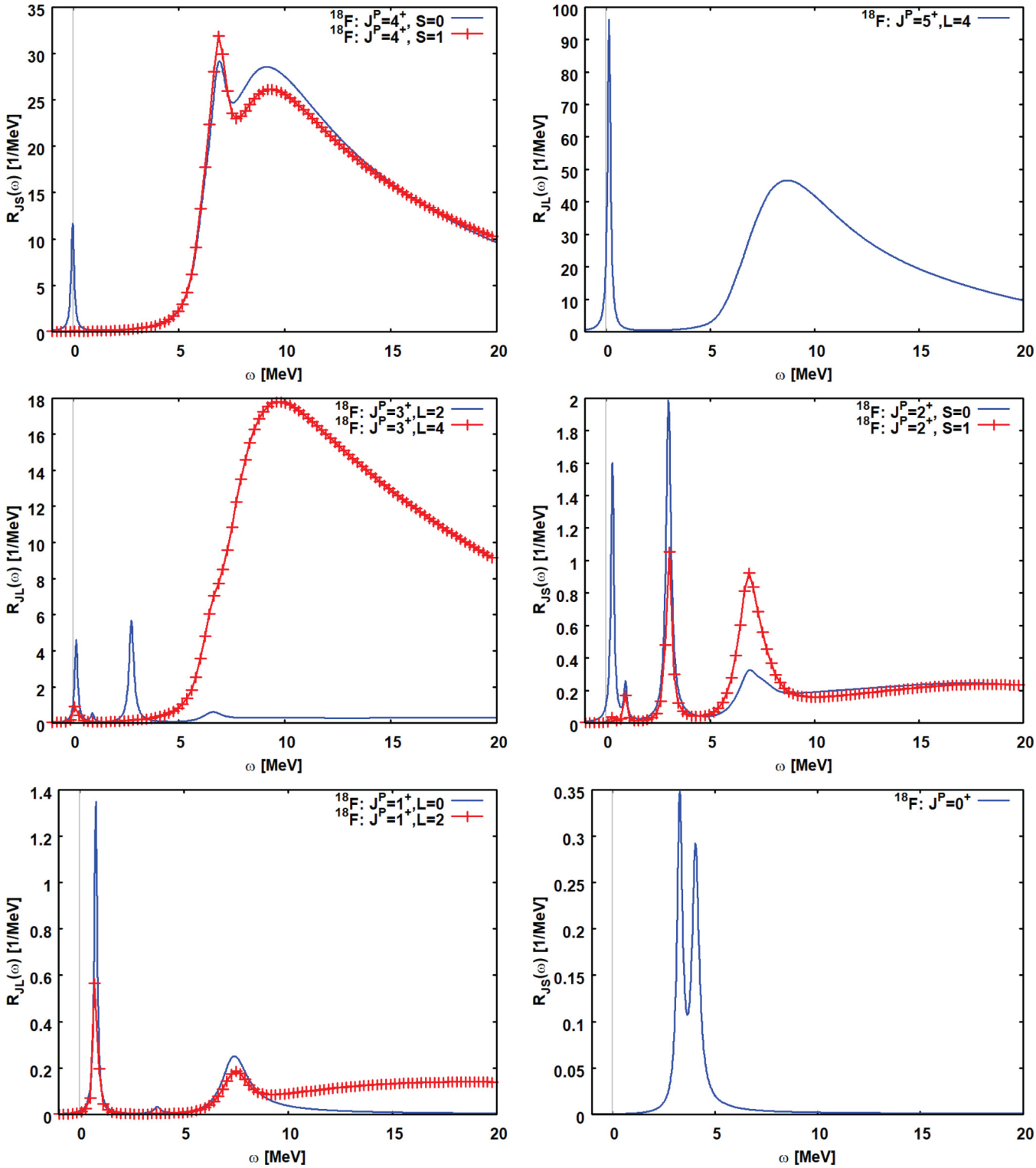


FIG. 6. QRPA response functions for $^{18}$O → $^{18}$F transitions. Results for the multipole transition operators $T_{\mathrm{LSJM}} = (\frac{r}{R_d})^L[\boldsymbol{\sigma}^S \otimes Y_L]_{JM}\tau_+$ are shown where $R_d = 2.74$ fm corresponds to the half-density radius of $^{18}$O.

of the two observed $J^P = 0^+$ states at $E_x = 1042$ keV and $E_x = 4753$ MeV, respectively. Above $E_x \sim 5.6$ MeV, the proton continuum is populated, thus leading to particle unstable states.

Overall, the rather complex spectrum is described surprisingly well by the QRPA calculations, which is especially worthwhile since global model parameters were used without any attempt at fine-tuning.

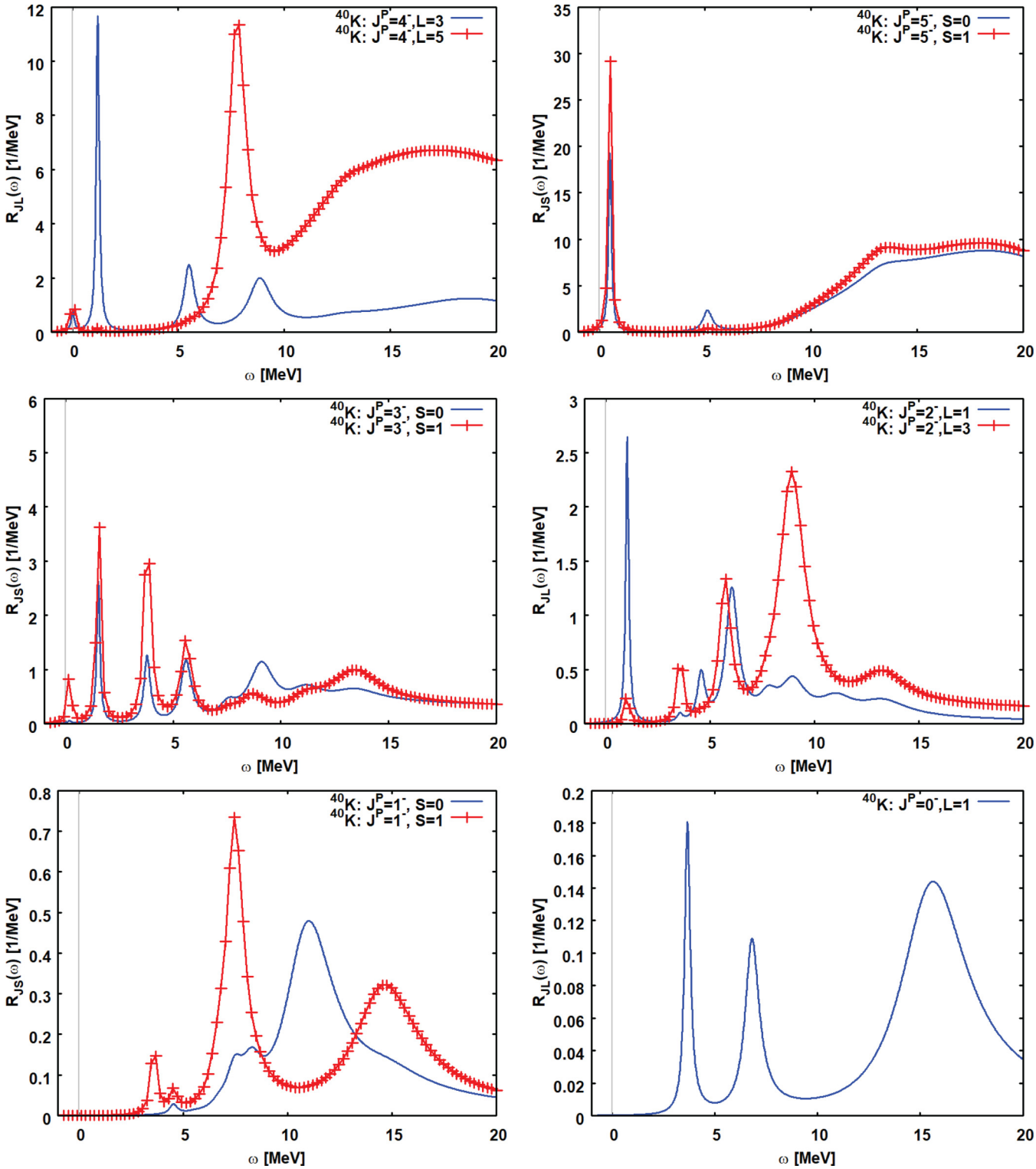


FIG. 7. QRPA response functions for $^{40}$Ca $\rightarrow$ $^{40}$K transitions. Results for the multipole transition operators $T_{\mathrm{LSJM}} = (\frac{r}{R_d})^L [\sigma^S \otimes Y_L]_{JM} \tau_-$ are shown where $R_d = 3.72$ fm corresponds to the half-density radius of $^{40}$Ca.

#### 4. *Charge-changing response functions for* $^{40}$Ca

Since $^{40}$Ca is a (double-magic) $N = Z$ nucleus, protons and neutrons are occupying the same single-particle orbitals. Therefore, also the odd-odd daughter nuclei $^{40}$K and $^{40}$Sc are of a mirrorlike level structure, reflecting the almost conserved isospin symmetry. The low-energy part of both excitation branches is determined by hole states in the $(2s, 1d)$ shell and particle states in the $(2p, 1f)$ shell. Thus, negative-parity states with $J^P = 0^- \cdots 5^-$ will prevail in the spectra. Ex-

perimentally, one finds for both daughter nuclei a $J^P = 4^-$ ground state. In $^{40}$K, a triplet of $J^P = 3^-, 2^-, 5^-$ states is seen at $E_x = 29, 80$, and 891 keV. Another $J^P = 2^-, 3^-$ doublet is found at $E_x = 2047, 2070$ keV and the first $J^P = 1^-$ occurs at $E_x = 2104$ keV. At $E_x = 2626$ keV, a $J^P = 0^-$ state is seen. However, there are also positive-parity intruder states which, similar to the $A = 18$ systems, indicate the lack of perfect shell closures. Above $E_x \sim 2.5$ MeV, a dense spectrum of positive- and negative-parity states is observed. The spectrum of $^{40}$Sc is less well known, but tentative assignments of spins and parity indicate at least for the ground-state multiplet a very similar $J^P = 4^-, 2^-, 3^-, 5^-$ level sequence with a comparable spacing.

Using the same scheme as in the previous case, also here HFB single quasiparticle energies, pairing amplitudes, and wave functions for $^{40}$Ca have been used to construct the polarization propagators. The QRPA spectra for $^{40}$K are shown in Fig. 7. The $A = 40$ ground-state multiplets are satisfactorily described: A $J^P = 4^-$ ground state is obtained and we observe the level sequence $J^P = 3^-, 5^-, 2-$ at $E_x = 302, 501, 1008$ keV. As in the data, $J^P = 0^-, 1^-$ states are found at higher energies, namely $E_x = 3726$ keV and $E_x = 3562$ keV. Positive-parity states are expected to occur at very high energy, in fact beyond the continuum thresholds. The reason is that the $^{40}$Ca HFB ground state is given by a perfect double-magic shell closure. However, as discussed in Refs. [34,35], core polarization will modify that picture by dissolving the shell closures in $^{40}$Ca on a level of about 10 to 15% and intruder positive-parity states may be present also at low energy.

We emphasize again that the same EDF was used as in the $A = 18$ calculations, refraining from parameter adjustments. As is typical for mean-field-based theories, in this case the larger mass of the parent nucleus led to an even better agreement with data. Thus, we may conclude that the QRPA approach provides a quite reliable description of SCE spectra.

### B. Optical potential and elastic scattering

A key issue for understanding heavy-ion reactions on a quantitative level is the proper treatment of ion-ion interactions. Their paramount role is evident by considering the huge total reaction cross sections, which reflect the importance of absorption of the incoming flux into a multitude of reaction channels. Because of the lack of elastic scattering data, empirical optical potentials are not available for the projectile-target systems under scrutiny. Thus, we calculate the optical potential fully microscopically in a folding approach. The HFB ground-state densities discussed above are folded with the $NN$ $T$-matrix interaction, including both the isoscalar and isovector components. Because heavy-ion scattering is a strongly absorptive process, elastic scattering and peripheral inelastic reactions are mainly sensitive to the nuclear surface regions of the interacting nuclei. Thus, to a very good approximation, in-medium modifications of interactions can be neglected in the elastic ion-ion interactions and we are allowed to use the free-space $NN$ $T$ matrix as the dominant leading-order impulse approximation. In the numerical calculations, the $NN$ $T$ matrix derived by Franey and Love [36] was used,

TABLE II. Defining quantities of the double-folding optical potential for the systems $^{18}\mathrm{O} + ^{40}\mathrm{Ca}$ and $^{18}\mathrm{O} + ^{116}\mathrm{Sn}$ at $T_{\mathrm{lab}} = 270$ MeV. Volume integrals per projectile and target nucleon numbers are denoted by $I_0/N$. HFB ground-state densities and the free-space $NN$ $T$-matrix interaction obtained from Ref. [36] were used.

| $U_{\mathrm{opt}}$ | Target | $I_0/N$ [MeV fm$^3$]/$N$ | $\sqrt{\langle r^2 \rangle}$ [fm] |
|---|---|---|---|
| Re$U_{\mathrm{opt}}$ | $^{40}$Ca | –439.71 | 4.75 |
| Im$U_{\mathrm{opt}}$ | $^{40}$Ca | –319.37 | 4.61 |
| Re$U_{\mathrm{opt}}$ | $^{116}$Sn | –543.09 | 5.70 |
| Im$U_{\mathrm{opt}}$ | $^{116}$Sn | –503.33 | 5.58 |

extrapolated down to the present energy region. The approach is used for calculating the real and the imaginary parts of the optical potentials in the incident and the exit channels. The Pauli principle is taken care of by the pseudopotential approach in local momentum approximation [17]. Distorted waves are obtained by solving the Schrödinger equation with these microscopically derived optical potentials as discussed in Sec. IV.

Characterizing quantities like volume integrals (per nucleon) and root-mean square radii are found in Table II, for the $^{18}\mathrm{O} + ^{40}\mathrm{Ca}$ and $^{18}\mathrm{O} + ^{116}\mathrm{Sn}$ systems at the beam energy $T_{\mathrm{lab}} = 270$ MeV.

Corresponding reaction cross sections are represented in Fig. 8, as a function of the beam energy. In Ref. [21], Khoa *et al.* have used the double-folding approach in a systematic study of $^{12}\mathrm{C} + ^{12}\mathrm{C}$ and $^{16}\mathrm{O} + ^{16}\mathrm{O}$ elastic scattering in about the same range of incident energies. For those lighter systems, they found total reaction cross sections of about 1.5 to 1.8 b, which is in fair agreement with our results for the heavier target-projectile combinations. In Ref. [37], the fusion cross section of $^{16}\mathrm{O} + ^{40}\mathrm{Ca}$ has been measured resulting in values of about $\sigma_f \sim 1.2$ b at energies below $T_{\mathrm{c.m.}} \sim 100$ MeV. Since $\sigma_f$ is only a part of the total reaction cross, that value should be considered as a lower limit for $\sigma_{\mathrm{abs}}$, thus supporting the re-

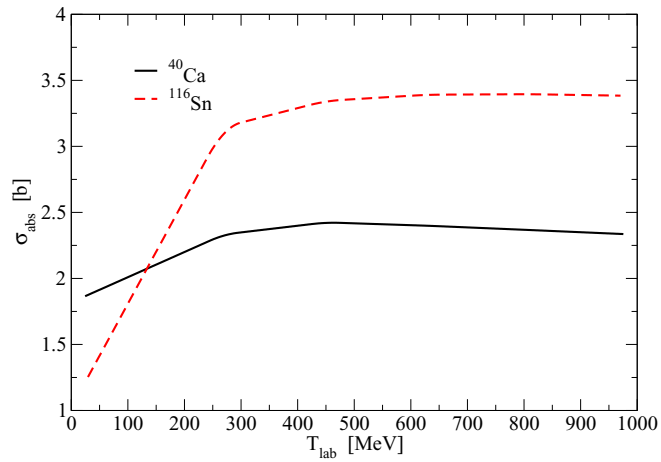


FIG. 8. Reaction cross sections as a function of beam energy, for the systems $^{18}\mathrm{O} + ^{40}\mathrm{Ca}$ and $^{18}\mathrm{O} + ^{116}\mathrm{Sn}$. The results are in quantitative agreement with those of the double-folding investigations by Khoa *et al.* [21].

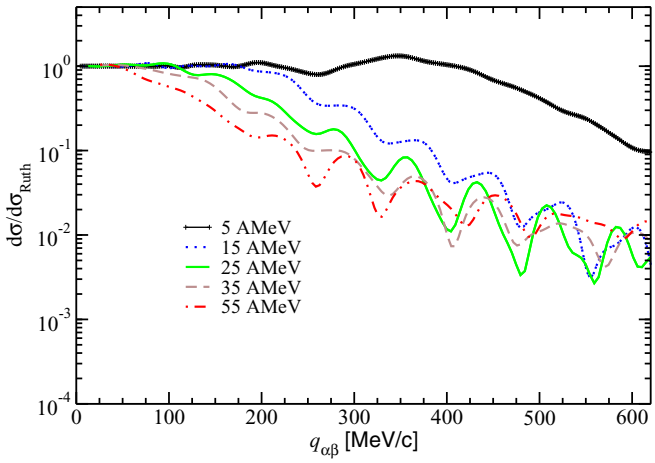


FIG. 9. Elastic scattering angular distributions for $^{18}O + ^{40}Ca$ at several beam energies, normalized to the Rutherford cross section, are shown as a function of the momentum transfer. The momentum range corresponds up to twice the Fermi momentum at central nuclear density, $q_{\alpha,\beta} \approx 600$ MeV/c.

sults of Fig. 8. We emphasize, however, that finally the ion-ion potentials have to be adjusted once elastic scattering data will be available. Results for the elastic scattering cross sections, normalized to the Rutherford cross section, are shown in Fig. 9 for the $^{18}O + ^{40}Ca$ system at different beam energies. At extremely small momentum transfer (i.e., extreme forward scattering angles) it is dominated by pure Coulomb scattering, but beyond $q_{\alpha\beta} \approx 200$ MeV/c, the short-range nuclear parts are taking over.

### C. Distortion effects in heavy ion SCE cross sections

Following the reaction and nuclear structure formalism outlined above, numerical calculations of single charge exchange cross section have been performed [38]. Form factors are derived by folding the transition densities with the projectile-target residual charge exchange interaction where the momentum representation is used [18]. In order to maintain self-consistency as much as possible, we use the same 2QP isovector interaction as in the nuclear structure calculations. The operator structure includes spin-dependent and spin-independent direct and exchange central interactions, together with second-rank tensor terms. The $NN$ spin-orbit interactions have been neglected. The procedure follows closely the approach used successfully in our previous investigations of SCE reactions [8–11,38].

The closest resemblance to nuclear $\beta$ decay processes is found in pure Gamow-Teller (spin-isospin flip with $J^P = 1^+$) or pure Fermi (isospin flip with $J^P = 0^+$) excitations, respectively. However, strong interaction processes are less selective on multipolarities than weak interactions. Moreover, because of the peripheral character of inclusive heavy-ion reactions, very often transition of higher angular momentum transfer are favored. Thus, heavy-ion SCE reactions enable to probe the whole spectrum of Gamow-Teller-like spin-isospin-flip and Fermi-like isospin-flip multipole transitions, discussed in the previous section, allowing us to study multipolarities

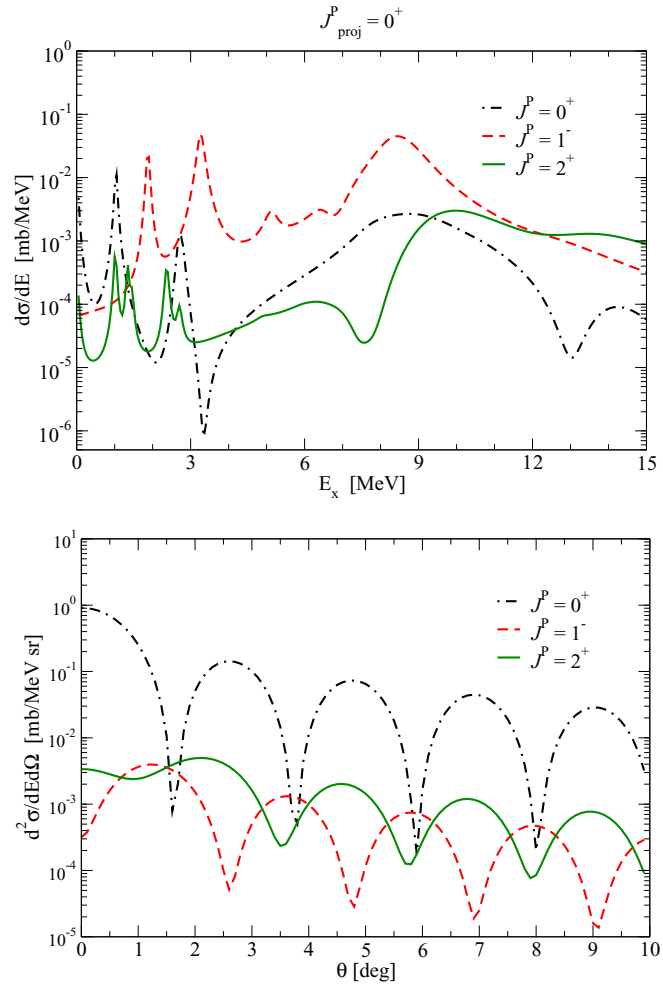


FIG. 10. DWBA cross section as a function of target excitation energy, integrated over the full angular range (top panel), and angular distribution for $E_x = 0$ MeV (bottom panel) for several multipoles, contributing to Fermi-like transitions in the target. Calculations are for the reaction $^{40}Ca(^{18}O, ^{18}F)^{40}K$ reaction at $T_{lab} = 270$ MeV using double-folding optical potentials and QRPA response functions.

suppressed otherwise in weak decay processes. From the theoretical discussion it is clear that distortion effects are playing a significant role in heavy-ion SCE reactions. Results for SCE single- and double-differential cross sections in full DWBA are shown in Figs. 10–12, for the reaction $^{18}O + ^{40}Ca \rightarrow ^{18}F + ^{40}K$ with $Q_{gs} = -2.97$ MeV. The complementary SCE reaction $^{18}O + ^{40}Ca \rightarrow ^{18}N + ^{40}Sc$ is kinematically suppressed because of the large $Q_{gs} = -28.22$ MeV.

For the Gamow-Teller (Fermi) case, we consider transitions leading to the $1^+$ ground state ($0^+$ excited state) of $^{18}F$ and populating several $^{40}K$ excited states, identified by the spin $J$ and the excitation energy $E_x = E_B^*$. For the present purpose, we neglect the small variations in excitation energy of the $^{18}F$ ground-state multiplet, treating the states as energetically degenerate with vanishing excitation energy. From Figs. 10–12, it is straightforward to note that $J^P = 1^+$ and $J^P = 0^+$ target transitions contribute significantly to the

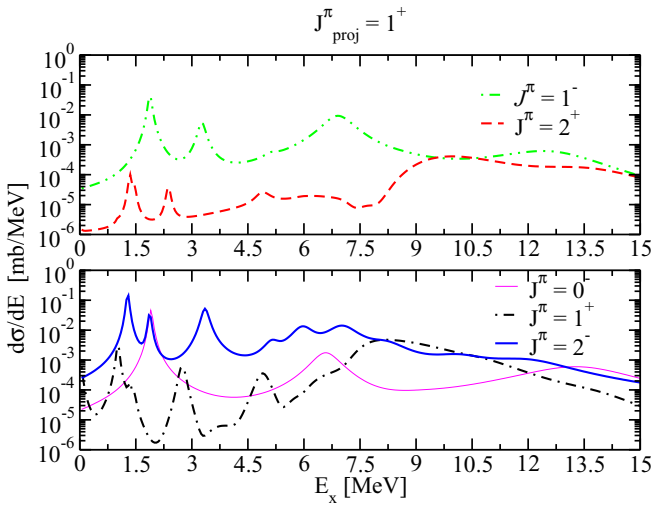


FIG. 11. DWBA cross section as a function of target excitation energy, integrated in the full angular range, for several multipoles, contributing to Gamow-Teller-like transitions, with natural parity (top panel) and unnatural parity (bottom panel), in the target. The system is the same as in Fig. 10, using again QRPA spectral distributions.

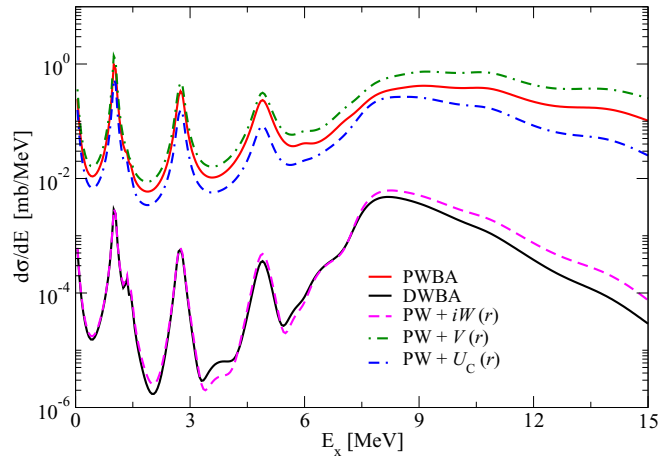


FIG. 13. Cross sections as a function of the target excitation energy, $E_x$, for the $J^P = 1^+$ transition, for the SCE reaction $^{40}$Ca($^{18}$O, $^{18}$F)$^{40}$K reaction at $T_{\rm lab} = 270$ MeV, integrated over the full angular range. The different curves show the effect of Coulomb potential [$U_C(r)$], of real [$V(r)$] and imaginary [$W(r)$] components of the optical potential, and of the full potential (DWBA), with respect to PWBA calculations. The system is the same as in the previous figures.

cross section at low excitation energies and dominate at small angles.

Having in mind to illustrate global features of heavy-ion SCE reactions, we will focus thereafter on pure Gamow-Teller excitations in both projectile and target. The results concerning distortion effects and the relation of the (physical) DWBA cross section to the plane wave counterpart and the $\beta$-decay matrix elements is to a large extent independent of the multipolarity, at least at small momentum transfer. Thus, without loss of generality, it is sufficient to consider a single multipolarity.

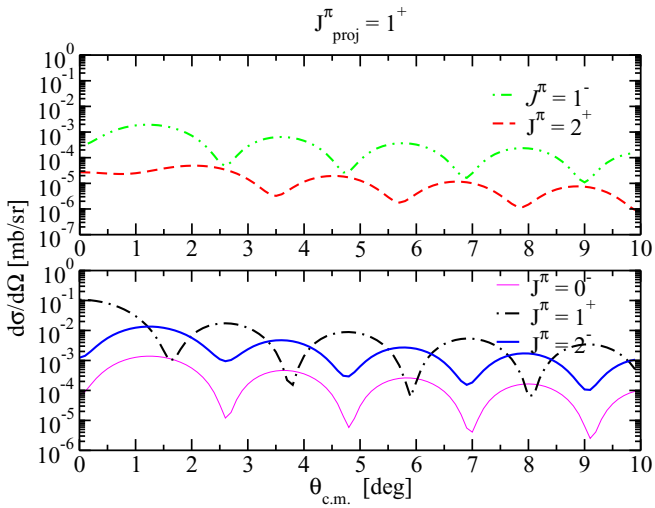


FIG. 12. DWBA angular distribution for $E_x = 0$ MeV, for several multipoles contributing to Gamow-Teller-like transitions, with natural parity (top panel) and unnatural parity (bottom panel), in the target. The system is the same as in Fig. 10.

In order to understand the influence of the elastic ion-ion interactions on SCE processes, we first disentangle the various contributions to the optical potentials. Figure 13 displays the ($^{18}$O, $^{18}$F(g.s.)) total cross section $\sigma_{\alpha\beta}$ as a function of the target excitation energy, integrated over the full angular range. Calculations are performed in the plane-wave Born approximation (PWBA), as well as considering separately the effects of Coulomb potential and of real and imaginary parts of the nuclear optical potential, and, finally, combining all these potentials in DWBA. Already at the PWBA level, one can appreciate the main excitation peaks contributing to $J^P = 1^+$ transitions in the target. With respect to the latter results, it is observed that the cross section decreases when the effect of the Coulomb repulsion is taken into account or increases when considering the contribution of the (attractive) real part of the nuclear optical potential. However, the most striking feature is the strong suppression, by about a factor 500–600, observed just taking into account the imaginary part of the optical potential, which essentially brings the cross section down to the value associated with the full DWBA calculation. This indicates that the DWBA result is mainly explained in terms of strong absorption effects, as expected in heavy-ion reactions, and justifies the strong absorption approach, underlying the black disk approximation to model the ion-ion initial- and final-state interactions (see Sec. V).

Moreover, the calculations show that absorption effects also affect the diffraction pattern of the nonelastic angular distributions: Under strong absorption conditions, the transition occurs effectively in the surface layers of the reacting nuclei which consequently is reflected in the structure of the angular distribution. The effect is most pronounced in transitions of low multipolarities.

The interplay between central and tensor terms of the effective interaction is investigated next. Results are shown

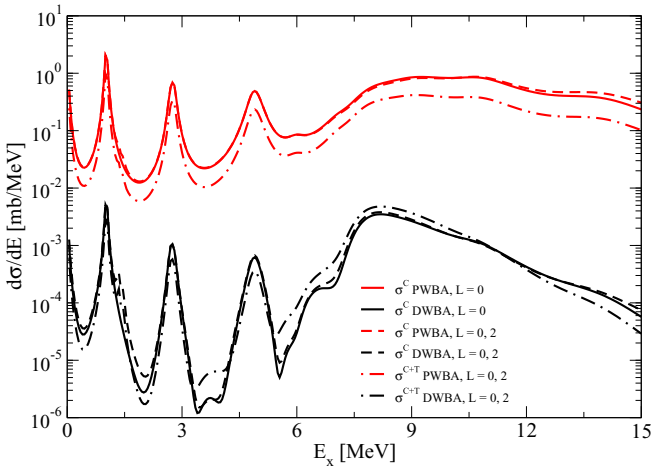


FIG. 14. Cross section as a function of the target excitation energy, integrated over the full angular range. The plot shows the effects of $L = 0, 2$ multipolarities, involved in $J^\pi = 1^+$ transition and of central and tensor components of nuclear interaction. Same system as in the previous figures.

in Figs. 14 and 15, together with the contributions associated with the two multipolarities ($L = 0, 2$) leading to $J^P = 1^+$ transitions. One can see that the central interaction contribution to the angle-integrated cross section is fully dominated by $L = 0$ transitions. The differential cross section, Fig. 15, is shown for the state at the lowest excitation energy ($E_x = E_B^* = 0$ MeV), that as discussed before is an intruder state for the $^{40}$K ground state. The same conclusion holds, as far as the small angles shown on the figure are concerned.

The tensor interaction is seen to slightly reduce the cross section in the PWBA case and, in the full DWBA calculations, for the main excitation peaks. Actually, as shown in Fig. 15, the tensor contributions also shift the cross section to larger angles, especially in the PWBA calculations, owing to the dominant role of $L = 2$ transitions in this case.

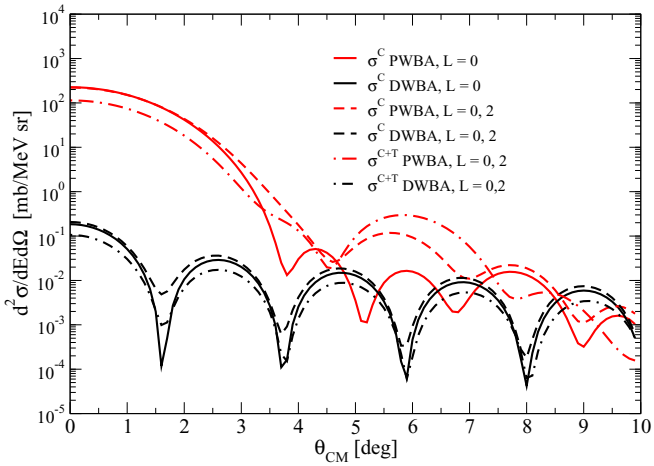


FIG. 15. Angular distribution for the target state at $E_x = 0$. The plot shows the effects related to central and tensor components of the nuclear interaction, for the two multipolarities allowed by $J^\pi = 1^+$ transitions: $L = 0, 2$. Same system as in the previous figures.

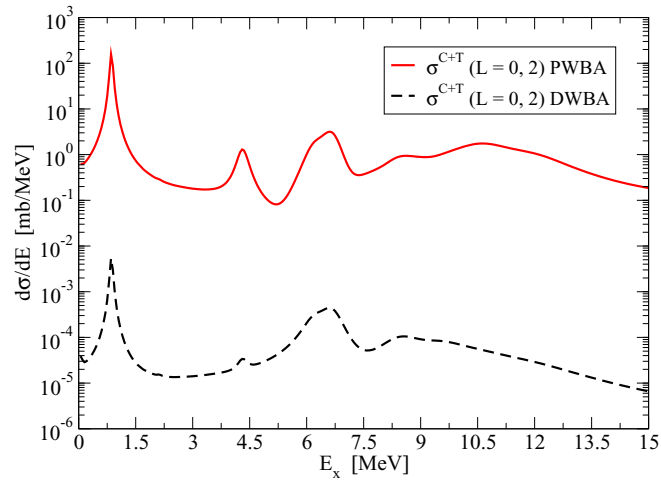


FIG. 16. Cross section as a function of the target excitation energy, integrated over the full angular range, for the reaction $^{18}$O + $^{116}$Sn at $T_{\rm lab} = 270$ MeV. Transitions leading to the $^{18}$F g.s. and to $J^\pi = 1^+$ states of the target are considered. PWBA and DWBA results are compared.

In Fig. 16, we show the angle-integrated cross section calculated for the system $^{18}$O + $^{116}$Sn, at the same beam energy $T_{\rm lab} = 270$ MeV. $J^\pi = 1^+$ transitions are considered in both projectile and target. The same QRPA approach, as described above for the $^{18}$O + $^{40}$Ca system, has been employed to evaluate the corresponding form factors. By comparing PWBA and DWBA results, one can notice that a smaller distortion factor is obtained for this reaction, with respect to the $^{40}$Ca target case. This trend is in agreement with the mass behavior predicted by the eikonal approximation; see Fig. 4.

Guided by the previous analysis, in the following we will consider, for the sake of simplicity, excitations corresponding to $L = 0$ and we will neglect the tensor part of the effective interaction.

### D. Cross-section factorization

As stressed in Sec. IV C, the case when the transition form factors, Eq. (A13), can be approximated by a Gaussian function is of a particular advantage for the separation of the distortion effects. This implies that the spatial transition densities contained in Eq. (A14) correspond to the multipole components of a Gaussian. Following the formalism outlined in Sec. IV C, we parametrize the microscopic transition densities, as obtained from our QRPA calculations for projectile and target, by a superposition of Gaussians.

Combining the results of projectile and target and neglecting the momentum dependence of the interaction form factor $V_{\rm ST}^C(p^2)$, which is quite flat in the low-momentum transfer range corresponding to $\theta \in [0^\circ, 10^\circ]$, one can finally extract the parameters ($R$ and $\sigma$) entering the expressions in Eqs. (50) and (51) for the full reaction amplitude in Born approximation, $M_{\alpha\beta}^{(B)}(\mathbf{p})$, which in the Gaussian representation can be evaluated analytically in closed form. Given $R_a(R_A)$ and $\sigma_a(\sigma_A)$ are the Gaussian parameters referring to the projectile (target) transition density, the combined, effective transition

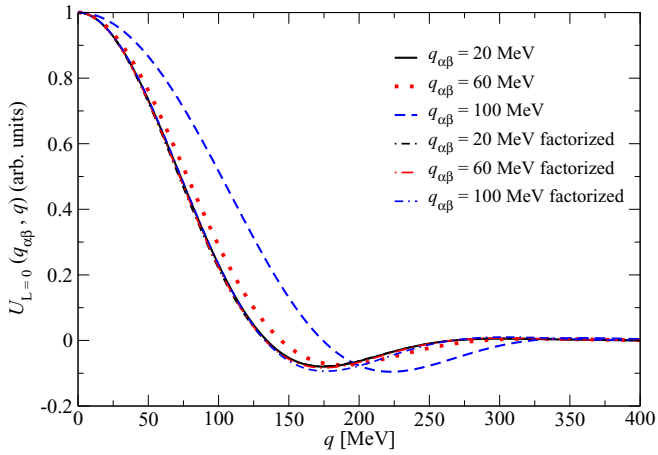


FIG. 17. Comparison between the monopole component of the Gaussian reaction kernel, obtained in the separation ansatz, with $h_{\alpha\beta}(q)$ given by Eq. (59) (dashed lines), and in the full BD approximation (solid lines). Different values of $q_{\alpha\beta}$ are considered. Some of the lines are difficult to distinguish because they are very close to each other.

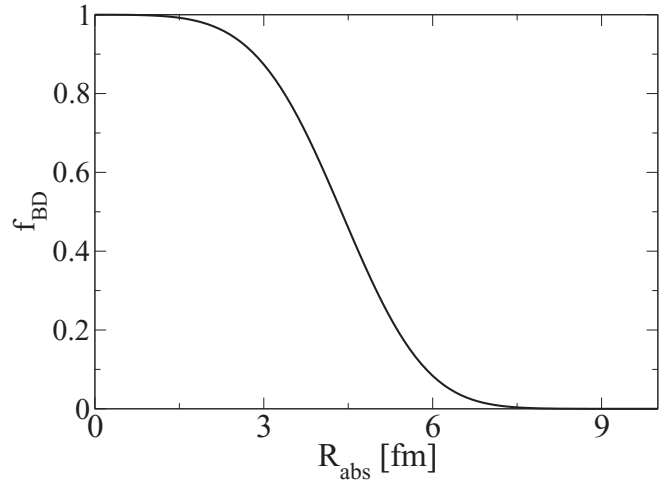


FIG. 18. Distortion factor as a function of $R_{\rm abs}$, for the separation function $h_{\alpha\beta}(q)$ corresponding to Eq. (59) (see text).

radius is $R^2 = R_a^2 + R_A^2$, and for the corresponding form factor width one finds $\sigma^2 = \sigma_a^2 + \sigma_A^2$. Then also the averaging over the orientation of the off-shell momentum $\mathbf{q}$, can be performed, leading to the reduced Born amplitude $\bar{M}^{(B)}_{\alpha\beta}(\mathbf{q}_{\alpha\beta}, q)$, which plays a central role for studies of distortion effects.

For the reaction under investigation, we find $R \approx 5\,$fm, $\sigma \approx 1.2\,$fm. Figure 17 shows the results obtained for the monopole term $U_{L=0}$, according to the full expressions Eqs. (41) and (42), or adopting the (partial) separation ansatz, as in Eqs. (52) and (59). One can observe that, whereas the separation ansatz works quite well for small values of $q_{\alpha\beta}$ (see, for instance, the results corresponding to $q_{\alpha\beta} \approx 20\,$MeV/c), important deviations from the exact results are seen for larger $q_{\alpha\beta}$ values.

Let us first consider the case of small momentum transfer ($q_{\alpha\beta} = 20\,$MeV/c). Using Eq. (63), the distortion factor $f_{\rm BD} = |1 - n_{\alpha\beta}|^2$ is readily obtained in the black disk approximation.[2] This is shown in Fig. 18 as a function of the absorption radius $R_{\rm abs}$. Here, the results obtained with the full expression of $h(q)$, as given in Appendix D, practically coincide with the approximate expressions, Eqs. (59) and (60). Guided by the total reaction cross section obtained numerically by the quantal partial wave method ($\sigma_{\rm abs} \simeq 2.14\,b$, see Fig. 8), we adopt $R_{\rm abs} = \sqrt{(}\sigma_{\rm abs}/\pi) \approx 8\,$fm. Correspondingly, the suppression factor is found to be $f_{\rm BD}(\text{analytical})|_{\substack{E_x=0\\ \theta=0}} \simeq 8.14 \times 10^{-4}$, in good agreement with the numerical DWBA/PWBA result, $f_{\rm BD}(\text{numerical})|_{\substack{E_x=0\\ \theta=0}} \simeq 8.35 \times 10^{-4}$, as it can be extracted from the ratio between DWBA and PWBA calculations at zero angle. As already anticipated above, owing to the important effects associated with the imaginary part of the optical potential, the black disk assumption represents quite well the distortion effects predicted by the full DWBA calculations. Figure 19 shows the distortion factor $f_{\rm BD}$, extracted by the ratio of DWBA and PWBA forward cross sections for the systems $^{18}\text{O} + ^{40}\text{Ca}$ and $^{18}\text{O} + ^{116}\text{Sn}$, as a function of the beam energy. The distortion factor drops sharply at low beam energy, despite the smaller absorption cross section seen in Fig. 8. This indicates that at beam energies close to the Coulomb barrier the BD assumption is lacking the additional suppression effects coming from the Coulomb barrier. However, as one can see on Fig. 19, at higher energy the distortion factor is increasing rather slowly and a quite good general agreement with the results obtained within the eikonal approximation, Fig. 4, is observed. Hence, at energies well above the Coulomb barrier, DWBA and PWBA forward angle cross sections are related to a good approximation by scaling factors, depending only moderately on the incident energy.

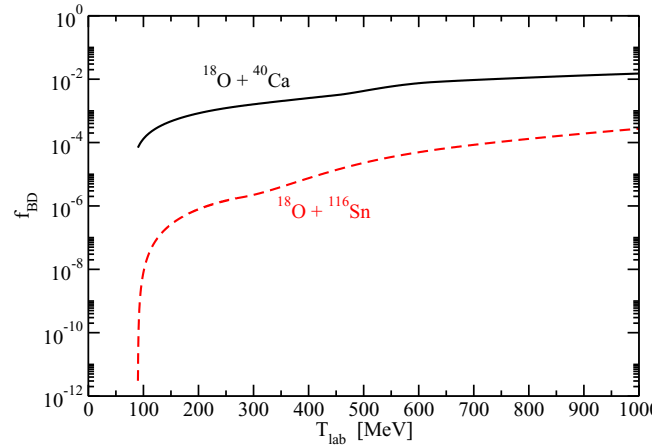


FIG. 19. The distortion factor $f_{\rm BD}$ is displayed as a function of the beam energy for two reaction systems: $^{18}\text{O} + ^{40}\text{Ca}$ and $^{18}\text{O} + ^{116}\text{Sn}$. The results were obtained numerically by the ratio of the quantum mechanical DWBA and PWBA forward angle cross sections.

[2]This relation is reminiscent of the aforementioned relation of the on-shell distortion coefficient to the elastic $S$ matrix; see Sec. V B.

The question may arise on the range of validity of the separation ansatz at finite momentum transfer. Explicit calculations can be easily performed in the full BD approximation, Eq. (40), and with the approximations introduced in Eq. (43), considering the separation function given by Eqs. (59) and (60). The results confirm that the black disk approximation indeed accounts appropriately for the absorption effects with, however, as a few caveats. So, as to be expected, we find that the scaling factor generally depends on $q_{\alpha\beta}$, limiting, e.g., the separation ansatz of Eq. (60) to low-momentum transfers up to $q_{\alpha\beta} \approx 50$ MeV/c. The description is improved by using the partial separation ansatz of Eq. (59), which extends the range of validity over a larger region of $q_{\alpha\beta}$ values, in the present case to momentum transfers of about 100 MeV/c.

The results discussed here for $E_x = 0$ can be extended easily to transitions leading to other excited states. We conclude that the full cross-section factorization is generally valid for small momentum transfer, i.e., in the case of low-energy excitations and forward angles. Under these conditions, it is possible to isolate in the SCE reaction amplitude the contribution of the Born amplitude, as done in Eq. (45). This is particularly important because it allows us to access direct information on the nuclear matrix elements, which are linked, in turn, to $\beta$-decay strengths, as discussed in Appendix F.

## VII. SUMMARY AND OUTLOOK

Heavy-ion reactions are of wide interest by their own because of the possibility to explore several excitation mechanisms by the same experiment. Charge-changing reactions, in particular, open unprecedented perspectives for detailed nuclear structure investigations of the many-body dynamics underlying also $\beta$-decay processes. In this paper, we have presented a revised approach to the theoretical modeling of nuclear SCE reactions. In a strictly microscopic picture, we have reformulated the reaction dynamical aspects in the framework of DWBA theory. Central and rank-2 tensor interactions were considered. In momentum representation, the reaction amplitude was separated formally into projectile and target transition form factors and the distortion coefficient, accounting for ISI and FSI ion-ion interactions.

HFB theory is used to describe the projectile and target ground states. The charge changing nuclear excitations were described by correlated 2QP configurations including residual quasiparticle interactions. Effects beyond mean-field dynamics were treated by introducing dynamical self-energies of a universal character. Thus, an extended QRPA approach was obtained. The QRPA problem is solved by direct solution of the Dyson equation, which is closely connected to the polarization propagators formalism. Nuclear response functions were introduced as the appropriate method for investigating charge-changing external fields which in the present context are provided by the isovector $NN$ projectile-target interactions.

The nuclear structure approach has been illustrated in calculations for charge-changing excitations of $^{18}$O and $^{40}$Ca. Response functions for multipole operators, intimately connected to weak interactions at low momentum transfer, have been discussed. As illustrative—and typical—examples, results for both $\tau_\pm$ branches have been presented. The $^{18}$F spectra could be reproduced satisfactorily well. An even better agreement with spectral data was obtained for the heavier system $^{40}$K.

Our previous investigations of heavy-ion SCE reactions have shown that fully quantum mechanical DWBA calculations with microscopic nuclear structure input describe observed cross sections quantitatively. Thus, from the theoretical side we have a powerful and successful toolbox at hand. However, for the direct extraction of spectroscopic quantities from measured cross sections, a separation of reaction and nuclear dynamics contributions is of great advantage. In this respect, a central goal of our investigation was to explore in detail the interplay of reaction and nuclear structure aspects in heavy-ion SCE cross section, aiming at identifying the conditions under which the two parts factorize, thus giving access to nuclear matrix elements relevant for $\beta$-decay processes. We note that this point has been widely investigated for reactions involving light projectiles (such as protons or $^3$He) at energies of a few hundred MeV per nucleon and found to be a quite useful tool to extract direct information on the $\beta$-decay strength of the target. Here, we could show that heavy-ion reactions of a few tens of MeV per particle are in principle as well suited for such explorations.

Performing explicit calculations for the reaction $^{18}\mathrm{O} + {}^{40}\mathrm{Ca}$ at $T_{\mathrm{lab}} = 15$ A MeV, we have shown that in heavy-ion reactions the distortion effects are strongly amplified, where the imaginary part of the nuclear optical potential is playing the major role. Indeed, SCE cross sections obtained with only the imaginary potential (i.e., neglecting real part and Coulomb interaction) in the initial- and final-state elastic ion-ion interactions coincide almost perfectly with results by full DWBA calculations. Thus, the distortion effects are in fact mainly absorption effects which are well reproduced in the strong absorption limit by the black disk approximation. Within such a scheme, we have worked out a factorization of the reaction cross section which is well suited for reactions characterized by small momentum transfer.

The investigations have shown that heavy-ion SCE reactions indeed allow us to extract from the forward-angle cross section, i.e., at small momentum transfer, a direct information on the product of the $\beta$-decay strengths in projectile and target. Hence, also in the case of heavy-ion reactions, we are led to define a "unit" cross section, which allows us to relate the SCE differential cross section to the $\beta$-decay strengths. For a given projectile, calculations performed in the black disk approximation suggest a $\approx 1/A$ dependence of the distortion factor on the target mass. The dominant role played by ISI and FSI demands for studies of elastic scattering. Angular distribution data in at least one of the involved channels would be of high importance as a countercheck of the accuracy of the microscopically derived ion-ion potentials which are central parts of the presented approach.

Eikonal theory provides an elegant approach to investigate universal aspects of the mass and energy dependences of distortion effects. These kinds of predictions are of interest especially for estimates of yields to be expected in future experiments. The intentions of the present eikonal studies is to encircle global trends and variations of cross sections.

We emphasize again that for a quantitative analysis of a given reaction a fully quantum mechanical calculation, as indicated, will be the preferred method. Here, we have used physically meaningful but schematic descriptions for the mass and energy dependences of the input quantities, as there are optical potentials and transition potentials. Both quantities were approximated by Gaussian form factors.

Within the Gauss-eikonal approximation, the mass and energy dependences of the distortion factor were investigated in the strong absorption limit. An attractive feature of GEA approach is that it allows us to connect the phenomenological concept of black disk (or black sphere) scattering to the microscopic background. The results for the distortion factor are clearly indicating certain constraints on heavy-ion SCE reactions: The magnitude of the cross sections will depend critically on the projectile-target combination. At fixed energy, systems with low total mass are favored, meaning that, e.g., an increase of the target mass will result in a decreasing cross section. The same is true for a variation of the projectile mass. However, this mass effect can be compensated to a large extent by varying the energy because the coefficient $f_{\rm BD}$ increases rapidly with incident energy.

Broad space was given to a formulation covering reaction and nuclear structure aspects on the same footing. By practical considerations, the main weight was laid on reactions at energies well above the Coulomb barrier. Such reactions are of high interest for currently active experiments, e.g., within the NUMEN project at LNS Catania [12]. The theoretical results, however, apply to other choices of projectile-target combinations and energy as well. These developments of the theory of heavy-ion SCE reactions open new interesting perspectives for experiments involving unstable nuclei [39] and for studies of double charge exchange (DCE) reactions. The extension to heavy-ion DCE reactions will be the topic of a forthcoming paper. In fact, with appropriate extensions, the methodology developed in this work is a suitably entry point for investigations of second-order processes as the heavy-ion DCE reactions, allowing us to establish their possible relation to double-$\beta$-decay processes.

## ACKNOWLEDGMENTS

Part of this work was done during the visits of H.L. to LNS Catania. The warm hospitality of the NUMEN group and the financial support by the NUMEN project are gratefully acknowledged. We wish to thank F. Cappuzzello and M. Cavallaro for fruitful discussions. This project has received funding from the European Union's Horizon 2020 research and innovation programme under Grant Agreement No. 654002 and from the Spanish Ministerio de Ciencia, Innovacion y Universidades and FEDER funds under Project No. FIS2017-88410-P.

## APPENDIX A: SECOND QUANTIZATION AND ONE-BODY TRANSITION DENSITIES

The spacial multipole components of the transition operator, Eq. (13), lead to the irreducible tensor operators (for $S = 0, 1$)

$$R_{\rm LSJM}(\mathbf{r},\boldsymbol{\sigma}) = \sum_{M_L,M_S} (LM_LSM_S|JM) i^L Y_{LM_L}(\hat{\mathbf{r}}) \big(\sigma_{M_S}\big)^S = [i^L Y_L(\hat{\mathbf{r}}) \otimes (\boldsymbol{\sigma})^S]_{JM}, \tag{A1}$$

where $Y_{LM_L}$ denotes spherical harmonics functions. In the second quantization, the one-body transition matrix elements for $n \to p$ transitions are given by

$$U^{STLM_L}_{j_p m_p j_n m_n}(p^2) = \sum_{JM} (LM_LSM_S|JM) \langle j_p m_p | j_L(pr) \times R_{\rm LSJM}(\mathbf{r},\boldsymbol{\sigma}) \tau_+ | j_n m_n \rangle, \tag{A2}$$

where $j_L(x)$ are Bessel functions. For $p \to n$ transitions, one can write a similar expression, exchanging $n$ and $p$ indices and replacing $\tau_+$ by $\tau_-$. After we apply the Wigner-Eckardt theorem [20], the matrix elements separate into a Clebsch-Gordan coefficient and a reduced matrix element. This allows us to perform the summation over the proton and neutron magnetic quantum numbers, leading to the one-body transition density operators

$$A^\dagger_{JM}(j_p j_n) = \sum_{m_p m_n} (j_p m_p j_n m_n | JM) a^\dagger_{j_p m_p} \tilde{a}_{j_n m_n}, \tag{A3}$$

where $\tilde{a}_{jm} = (-)^{j+m} a_{j-m}$ denotes the conjugated operator. The proton-neutron and the neutron-proton particle-hole operators are related by Hermitian conjugation,

$$A^\dagger_{JM}(j_n j_p) = (-)^{J+M} A_{J-M}(j_p j_n), \tag{A4}$$

reflecting charge-conjugation symmetry. The reduced isovector matrix elements is

$$\bar{U}^{LSJ}_{j_p j_n}(p^2) = \frac{\sqrt{2}}{\hat{J}} \langle \ell_p s_p j_p || j_L(pr) R_{LSJ} || \ell_n s_n j_n \rangle, \tag{A5}$$

where $\hat{J} = \sqrt{2J+1}$ and $s_p = s_n = \frac{1}{2}$. The factor $\sqrt{2}$ results from the isospin structure of the isovector nucleon-meson vertices. These steps lead to the representation of the transition operators in terms of irreducible tensor components of conserved total angular momentum $J$

$$\sum_{m_p m_n} U^{STLM_L}_{j_p m_p j_n m_n}(p^2) a^\dagger_{j_p m_p} a_{j_n m_n} = \sum_{JM} (LM_LSM_S|JM) \bar{U}^{LSJ}_{j_p j_n}(p^2) A^\dagger_{JM}(j_p j_n). \tag{A6}$$

Thus, using second quantization, the transition operator becomes

$$\mathcal{R}_{\rm ST}(\mathbf{p}, a^\dagger a) = \sum_{LM_L JM} Y^*_{LM_L}(\hat{\mathbf{p}}) (LM_LSM_S|JM) \sum_{j_p,j_n} \big\{ \bar{U}^{LSJ}_{j_p j_n}(p^2) A^\dagger_{JM}(j_p j_n) + \bar{U}^{LSJ}_{j_n j_p}(p^2) A^\dagger_{JM}(j_n j_p) \big\}. \tag{A7}$$

The target transition form factors are now given as

$$F^{(AB)}_{SM_S}(\mathbf{p}) = \sum_{\lambda_A\mu_A I_A N_A} Y^*_{\lambda_A\mu_A}(\hat{\mathbf{p}})(\lambda_A\mu_A SM_S|I_A N_A)\Bigg\{\sum_{j_p,j_n}\bar{U}^{\lambda_A S I_A}_{j_p j_n}(p^2)\langle J_B M_B|A^\dagger_{I_A N_A}(j_p j_n)|J_A M_A\rangle + \sum_{j_p,j_n}\bar{U}^{\lambda_A S I_A}_{j_n j_p}(p^2)\langle J_B M_B|A^\dagger_{I_A N_A}(j_n j_p)|J_A M_A\rangle\Bigg\} \tag{A8}$$

and accordingly in the projectile system. For a given reaction, only one of the terms in Eq. (A8) is effectively contributing to the transition: If, e.g., a $p^{-1}n$-type transition is occurring in the projectile, only the parts containing operators of $a^\dagger_n a_p$ structures give nonvanishing contributions while the complementary $a^\dagger_p a_n$ operator branch is only active in the target, and vice versa.

The spectroscopy of the charge exchange process is now contained in one-body transition density matrix elements defined as

$$D^{JM}_{j_c j_d}(J_f M_f, J_i M_i) = \langle J_f M_f|A^\dagger_{JM}(j_c j_d)|J_i M_i\rangle. \tag{A9}$$

The Wigner-Eckardt theorem leads to

$$D^{JM}_{j_c j_d}(J_f M_f, J_i M_i) = (-)^{J_f - M_f}\big(J_f M_f J_i - M_i|J - M\big)\bar{D}^J_{j_c j_d}(J_f, J_i) \tag{A10}$$

with the reduced one-body transition density

$$\bar{D}^J_{j_c j_d}(J_f, J_i) = \frac{1}{\hat{J}}\langle J_f||A^\dagger_J(j_c j_d)||J_i\rangle. \tag{A11}$$

If the parent state has $J_i = 0$, the result simplifies to

$$D^{JM}_{j_c j_d}(J_f M_f, 00) = \bar{D}^J_{j_c j_d}\delta_{JJ_f}\delta_{MM_f}. \tag{A12}$$

The same simplification is obtained for the case $J_f = 0$.

Obviously, the one-body transition densities are the elements of central importance for the spectroscopy of the charge exchange process. They are providing access to the many-body structure of the underlying nuclear wave functions. The evaluation of the one-body transition densities requires knowledge of the structure of the initial and final nuclear states, establishing the connection to nuclear structure theory.

By standard angular momentum coupling techniques, Eq. (A8) becomes

$$F^{(AB)}_{\mathrm{ST}}(\mathbf{p}) = \sum_{L,M_L,J_2,M_2}(J_A M_A J_B M_B|J_2 M_2)(LM_L SM_S|J_2 M_2) \times f^{(AB)}_{LSJ_2}(p^2) i^L Y_{LM_L}(\hat{\boldsymbol{p}}) \tag{A13}$$

and corresponding expressions are found for projectile transitions. In Eq. (A13), the reduced form factors $f^{(XY)}_{LSJ}$ have been introduced. The latter are related to the corresponding reduced radial transition densities $\rho^{(XY)}_{LSJ}$ by a Fourier-Bessel transform:

$$f^{(XY)}_{LSJ}(p^2) = \int_0^\infty dr r^2 \rho^{(XY)}_{LSJ}(r) j_L(pr). \tag{A14}$$

The total angular momentum transfer in the projectile and target system are given by $J_{1,2}$, defining the set of multipole components which are contributing to a given reaction leading from initial states $J_{a,A}$ to final states $J_{b,B}$. These relations are expressed by the first Clebsch-Gordan coefficient in the above equations. In accordance with the investigations of the previous section, these multipoles carry substructures given by the coupling of orbital ($L_{1,2}$) and spin ($S_{1,2}$) angular momentum transfers, as expressed by the second Clebsch-Gordan coefficients in Eq. (A13).

## APPENDIX B: ANGULAR MOMENTUM DECOMPOSITION OF THE REACTION KERNEL

The decomposition of the full reaction kernel and correspondingly the reaction amplitude relies on their decomposition into irreducible tensorial components. For that purpose, the product of the projectile and target form factors, Eq. (14), must be recoupled to total angular momentum. We use the addition theorem of spherical harmonics [20]

$$i^{L_1}Y_{L_1 m_1}(\hat{\mathbf{p}})i^{L_2}Y_{L_2 m_2}(\hat{\mathbf{p}}) = \sum_{LM_L}(-)^{\frac{L_1+L_2-L}{2}}\frac{\hat{L}_1\hat{L}_2}{\sqrt{4\pi}\hat{L}}(L_1 0 L_2 0|L0) \times (L_1 m_2 L_2 m_2|LM)i^L Y_{LM}(\hat{\mathbf{p}}). \tag{B1}$$

Then, for a central interaction, the product of nuclear form factors is obtained as

$$F^{(\alpha\beta)}_{\mathrm{ST}}(\mathbf{p}) = \sum_{J_1,M_1,J_2,M_2,L,M}(J_a M_a J_b M_b|J_1 M_1) \times (J_A M_A J_B M_B|J_2 M_2)(J_1 M_1 J_2 M_2|LM) \times i^L Y_{LM}(\hat{\boldsymbol{p}})F^{J_1 J_2}_{LS}(p^2), \tag{B2}$$

with the reduced multipole form factors

$$F^{J_1 J_2}_{LS}(p^2) = \sum_{L_1 L_2} A_{LS}(L_1 L_2, J_1 J_2) f^{(ab)}_{L_1 S J_1}(p^2) f^{(AB)}_{L_2 S J_2}(p^2). \tag{B3}$$

We have introduced the recoupling coefficients

$$A_{LS}(L_1L_2,\,J_1J_2) = (-)^{\frac{L_1+L_2-L}{2}}\frac{\hat{L}_1\hat{L}_2}{\sqrt{4\pi}\,\hat{L}}(L_1 0 L_2 0|L0)(-)^{L_2+J_1-L}W(L_1J_1L_2J_2;LS)\hat{J}_1\hat{J}_2, \tag{B4}$$

where $W(abcd;ef)$ is a Racah coefficient [20].

The rank-2 tensor component requires additional recoupling of the spin and orbital angular momentum operators in order to comply with the quadrupole character of the vertex. The resulting form factor can be cast into a form similar to Eq. (B2):

$$H^{(\alpha\beta)}_{\rm ST}(\mathbf{p}) = \sum_{J_1,M_1,J_2,M_2,L,M}(J_aM_aJ_bM_b|J_1M_1)(J_AM_AJ_BM_B|J_2M_2)(J_1M_1J_2M_2|LM)i^LY_{LM}(\hat{\mathbf{p}})H^{J_1J_2}_{L1}(p^2). \tag{B5}$$

The reduced form factors, however, are of a somewhat more involved structure:

$$H^{J_1J_2}_{L1}(p^2) = \sum_{L_1,L_2,L'}B_{LL'}(L_1L_2,\,J_1J_2)f^{(ab)}_{L_1 1J_1}(p^2)f^{(AB)}_{L_2 1J_2}(p^2). \tag{B6}$$

In this case, the recoupling coefficient is given by

$$B_{LL'}(L_1L_2,\,J_1J_2) = \sqrt{\frac{24\pi}{5}}(-)^{\frac{L_1+L_2-L}{2}}\frac{\hat{L}_1\hat{L}_2\sqrt{5}}{4\pi\,\hat{L}}\big(L_1 0 L_2 0|L'0\big)\big(L'020|L0\big)\hat{J}_1\hat{J}_2\hat{L}'\sqrt{5}\begin{Bmatrix}L_1 & 1 & J_1\\ L_2 & 1 & J_2\\ L' & 2 & L\end{Bmatrix}, \tag{B7}$$

where the object in the last line is a 9-$j$ symbol [20].

## APPENDIX C: GAUSSIAN FORM FACTORS AND MICROSCOPIC NUCLEAR STRUCTURE

The price paid for the advantage of the Gaussian approximation that the dependencies on the ion masses and sizes are directly accessible by closed-form expressions is that the connection to microscopic nuclear structure seems to be lost. However, by reinterpretation of the parametrical dependence on the yet-to-be-specified radius $R$, that connection can be restored under certain constraints. In leading order, the transition potential Eq. (14) is given by replacing the $NN$ $T$ matrix by a contact interaction where the strength if given by the momentum space amplitude at $p = 0$, i.e., the volume integral. Denoting the intrinsic projectile and target coordinates by $\mathbf{r}_{1,2}$, respectively, and the ion-ion relative coordinate by $\mathbf{r}$, the zero-range assumption implies $\mathbf{r}_1 + \mathbf{r} - \mathbf{r}_2 = 0$. For a contact interaction, the folding integral defining the transition potential reduces to the folding of the nuclear transition form factors. For that purpose, we assume that the intrinsic nuclear transitions $a \to b$ and $A \to B$ are described by Gaussian form factors

$$F_N(\mathbf{r}_N) = C_N e^{-\frac{1}{2\sigma_N^2}|\mathbf{r}_N-\mathbf{R}_N|^2}, \tag{C1}$$

where $N \in \{ab, AB\}$ $(N = 1, 2)$ and the normalization constant is chosen as $C_N = (\sqrt{2\pi}\sigma_N)^{-3}$ such that $F_N$ has a volume integral equal to unity. In coordinate space, we have to evaluate a folding integral of the type

$$F_{12}(\mathbf{r}) = C_1C_2\int d^3r_1 e^{-\frac{1}{2\sigma_1^2}(\mathbf{r}_1-\mathbf{R}_1)^2}e^{-\frac{1}{2\sigma_2^2}(\mathbf{r}_1+\mathbf{r}-\mathbf{R}_2)^2}. \tag{C2}$$

With the substitutions $\mathbf{x} = \mathbf{r}_1 - \mathbf{R}_1$ and $\boldsymbol{\rho} = \mathbf{r} + \mathbf{R}_1 - \mathbf{R}_2$, the integral becomes

$$F_{12}(\mathbf{r}) = C_1C_2\int d^3x e^{-\frac{1}{2\sigma_1^2}x^2}e^{-\frac{1}{2\sigma_2^2}(\mathbf{x}+\boldsymbol{\rho})^2}. \tag{C3}$$

The angle integrations lead to modified Bessel function of order $n = 0$. The remaining integration can be performed in closed form with the final result

$$F_{12}(\mathbf{r},\mathbf{R}) = \frac{1}{(\sqrt{2\pi}\sigma)^3}e^{-\frac{1}{2\sigma^2}(\mathbf{r}-\mathbf{R})^2}. \tag{C4}$$

The width is given by

$$\sigma^2 = \sigma_1^2 + \sigma_2^2, \tag{C5}$$

and the centroid radius is found as

$$\mathbf{R} = \mathbf{R}_1 - \mathbf{R}_2, \tag{C6}$$

which plays the role of a scale-defining quantity. Considered as classical mathematical objects, the vectors $\mathbf{R}_{1,2}$ are free parameters reflecting the nuclear scales. Thus, we use $R_{1,2} \sim A_{1,2}^{\frac{1}{3}}$. Since the relative orientation of the two centroid vectors is arbitrary, we use the averaging, resulting in $R^2 = R_1^2 + R_2^2 \simeq A_1^{\frac{2}{3}} + A_2^{\frac{2}{3}}$.

Within the above *zero-range* approximation, the transition potential, Eq. (46), is given by the superposition of a spin-scalar $(S = 0)$ and a spin-vector $(S = 1)$ component

$$U_G(\mathbf{r}) = \sum_{S=0,1,T=1} I_{\rm ST}B^{(ab,AB)}_{\rm ST}F^{(ab,AB)}_{12,ST}(\mathbf{r},\mathbf{R}_{\rm ST}), \tag{C7}$$

where $I_{\rm ST} \equiv V^{(C)}_{\rm ST}(p = 0)$ denotes the volume integral of the interaction. The crucial point is how to incorporate the underlying microscopic nuclear structure physics. The simplest, but rather schematic approach is to use projectile and target spectral distributions averaged over multipolarities. Such a solution is indicated above: The nuclear charge-changing spectral transition strengths for projectile and target are contained in $B^{ab,AB}_{\rm ST}$, obtained, e.g., by the response function formalism, Sec. VI A.

In a refined approach, the multipole structure of the form factors and spectral distributions should be combined explicitly. On a formal level, this is achieved by identifying $Y_{LM}(\hat{\mathbf{R}})$

as a dynamical quantity with an operator structure inducing intrinsic nuclear transitions. Formally, this is achieved by imposing the quantization conditions

$$Y_{LM}(\hat{\mathbf{R}}) \to \mathcal{Y}_{LM}(\Omega^\dagger) = \sum_{\lambda\kappa} b_\lambda(ab) b_\kappa(AB) [\Omega^\dagger_\lambda(ab)\Omega^\dagger_\kappa(AB)]_{LM}, \quad \text{(C8)}$$

i.e., a representation by the state operators $\Omega^\dagger_{\lambda,\kappa}$ of projectile and target, respectively. $\lambda$ and $\kappa$ include spin and orbital angular momenta. The coupling to good total angular momentum transfer $L$ is indicated. The expansion coefficients are given by nuclear multipole transition amplitudes. Thus, we have obtained a relation similar to the collective model approach to nuclear spectroscopy of Bohr and Mottelsen [40], widely used in the past for nuclear reactions. Thus, the essence of the Gaussian form factor is seen to separate the state-dependent transition form factors into a state-independent spatial form factor $U_{LM}(\mathbf{r})$, Eq. (48), and state-dependent amplitudes $b_\mu$, giving rise to the multipole spectral distributions

$$B_L^{(aA,bB)} = \langle bB|\mathcal{Y}_{LM}|aA\rangle \quad \text{(C9)}$$

and the multipole transition potentials

$$U^{aA,bB}_{ST,LM}(\mathbf{r}) = B_L^{(aA,bB)} I_{\rm ST} U_{LM}(\mathbf{r}), \quad \text{(C10)}$$

where the spectral amplitudes and the reduced form factors will depend in general also on the spin transfer $S$.

## APPENDIX D: GAUSSIAN APPROACH TO THE BLACK DISK DISTORTION FACTOR

As discussed, the separation function $h(q)$ is well approximated by the modified Gaussian in Eq. (56),

$$h(q) = e^{-\frac{1}{2}q^2\sigma^2} j_0(q\rho). \quad \text{(D1)}$$

The parameter $\sigma$ controls the slope of the momentum distribution around the momentum transfer $p = q_{\alpha\beta}$. The (off-shell) diffraction structure is determined by $\rho$. Thus, we have to evaluate the integral

$$n^{\rm BD} = \frac{2R_{\rm abs}}{\pi}\int_0^\infty dq j_0(qR_{\rm abs})\frac{\partial}{\partial q}[qh(q)], \quad \text{(D2)}$$

which is given explicitly by the three-parameter form

$$n^{\rm BD} = \frac{2R_{\rm abs}}{\pi}\int_0^\infty \frac{\sin(qR_{\rm abs})}{qR_{\rm abs}} e^{-\frac{1}{2}\sigma^2q^2} \times\left[-\frac{\sigma^2 q}{\rho}\sin(q\rho)+\cos(q\rho)\right]dq. \quad \text{(D3)}$$

The absorption radius, $R_{\rm abs}$, is fixed by the total reaction cross section. The integral can be performed in closed form, with the result

$$n^{\rm BD} = \frac{1}{2}\left\{erf\left[\frac{1}{\sqrt{2}\sigma'}(R'-\rho')\right]+erf\left[\frac{1}{\sqrt{2}\sigma'}(R'+\rho')\right]\right\} - \sqrt{\frac{2}{\pi}}\frac{\sigma'}{2\rho'}\left[e^{-\frac{1}{2\sigma'^2}(R'-\rho')^2}-e^{-\frac{1}{2\sigma'^2}(R'+\rho')^2}\right] \quad \text{(D4)}$$

expressed in terms of the scaled (dimensionless) quantities $R' = R_{\rm abs}/R$, $\sigma' = \sigma/R$, $q'_{\alpha\beta} = q_{\alpha\beta}R$, and $\rho' = \sqrt{1-\sigma'^4 q'^2_{\alpha\beta} + 2i\sigma'^2 q'_{\alpha\beta}\cos\gamma}$. $n^{\rm BD}$ is a complex-valued function, because it depends on the complex pseudoradius $\rho'$. Moreover, $n^{\rm BD}$ contains the full set of multipoles in $\mathbf{q}_{\alpha\beta}$. Typical results for $n^{\rm BD}$ are displayed in Fig. 18, for $q_{\alpha\beta}\approx 0$.

## APPENDIX E: DISTORTION COEFFICIENT IN EIKONAL APPROXIMATION

For wavelengths $\lambda \sim 1/k$ short against the scale $R_{\rm pot}$ of the interaction zone, i.e., $\xi = kR_{\rm pot} \gg 1$ semiclassical descriptions become an appropriate description for nuclear reactions. In the case considered here, we have $k_\alpha \simeq 10\,{\rm fm}^{-1}$ and $R_{\rm pot} \simeq 5$ fm (see Table II), leading to $\xi \simeq 40$. Thus, despite the rather low energy of $T_{\rm lab} = 270$ MeV, the kinematical conditions allow us to apply eikonal theory [41]. The distorted waves are given as

$$\chi^{(+)}_\alpha(\mathbf{k}_\alpha,\mathbf{r}) = e^{iS^{(+)}_\alpha(\boldsymbol{\rho},z)}e^{+i\mathbf{k}_\alpha\cdot\mathbf{r}}, \quad \text{(E1)}$$

$$\chi^{(-)*}_\beta(\mathbf{k}_\beta,\mathbf{r}) = e^{-iS^{(-)*}_\beta(\boldsymbol{\rho}',z')}e^{-i\mathbf{k}_\beta\cdot\mathbf{r}}, \quad \text{(E2)}$$

with the asymptotically in- and outgoing eikonals

$$S^{(+)}_\alpha(\boldsymbol{\rho},z) = \int_{-\infty}^{z} d\zeta[Q_\alpha(\boldsymbol{\rho},\zeta)-k_\alpha], \quad \text{(E3)}$$

$$S^{(-)*}_\beta(\boldsymbol{\rho}',z') = \int_{+\infty}^{z'} d\zeta(Q_\beta - k_\beta), \quad \text{(E4)}$$

where $z$ and $z'$ are directed along the channel momenta $\mathbf{k}_\alpha$ and $\mathbf{k}_\beta$, respectively. We have defined the local channel momenta

$$Q_\gamma(\boldsymbol{\rho},\zeta) = \sqrt{k_\gamma^2 - \frac{2m_\gamma}{\hbar^2}U_\gamma(\boldsymbol{\rho},\zeta)} \quad \text{(E5)}$$

and $\boldsymbol{\rho}$, $z$ are oriented such $z$ coincides with the direction of $\mathbf{k}_\alpha$ and $\boldsymbol{\rho}'$, $z'$ are taken accordingly with respect to $\mathbf{k}_\beta$. Hence, we identify $u^{(\pm)}_{\alpha,\beta} = e^{\pm iS^{(\pm)}_{\alpha,\beta}}$, leading to

$$\eta_{\alpha\beta} = u^{(-)*}_\beta u^{(+)}_\alpha = e^{i(S^{(+)}_\alpha - S^{(-)*}_\beta)} = e^{i\phi_{\alpha\beta}-\kappa_{\alpha\beta}}, \quad \text{(E6)}$$

where the (real) phase shift $\phi_{\alpha\beta}$ and the attenuation exponent $\kappa_{\alpha\beta}$ are given by the sum of the real and imaginary parts, respectively, of the eikonals. For small momentum and energy transfer, we may neglect the differences in the channel momenta and potentials. Furthermore, at small momentum transfer, $z$ and $z'$ may be assumed to be parallel. Under such conditions, the distortion amplitude is given by the (diagonal) distortion phase shift and attenuation exponent

$$\phi_\alpha(\boldsymbol{\rho}) \simeq \int_{-\infty}^{+\infty} d\zeta {\rm Re}[Q_\alpha(\rho,\zeta)] - k_\alpha, \quad \text{(E7)}$$

$$\kappa_\alpha(\boldsymbol{\rho}) \simeq \int_{-\infty}^{+\infty} d\zeta {\rm Im}[Q_\alpha(\rho,\zeta)]. \quad \text{(E8)}$$

As discussed in Sec. V B, in the strong absorption limit we need to consider $\phi_\alpha$ only in space regions where $\kappa_\alpha$ has decreased to $\mathcal{O}(1)$ or less. In those space regions, typically also ${\rm Re}(U_{\rm opt})$ is already of small magnitude. Hence, we can neglect terms of order $U_\alpha/k_\alpha^2$ and obtain the standard eikonal

expressions

$$\phi_\alpha(\boldsymbol{\rho}) \simeq -\frac{m_\alpha}{\hbar^2 k_\alpha}\int_{-\infty}^{+\infty} d\zeta \,\mathrm{Re}[U_\alpha(\rho,\zeta)], \tag{E9}$$

$$\kappa_\alpha(\boldsymbol{\rho}) \simeq \frac{m_\alpha}{\hbar^2 k_\alpha}\int_{-\infty}^{+\infty} d\zeta \,\mathrm{Im}[U_\alpha(\rho,\zeta)], \tag{E10}$$

usually combined in the profile function $\chi_\alpha = \phi_\alpha - i\kappa_\alpha$. For the present purpose, it is sufficient to consider the attenuation exponent. Assuming Gaussian form factors and spherical symmetry,

$$U_\alpha(r) = -U_0 e^{-r^2/R_U^2} - i\,W_0 e^{-r^2/R_W^2} \tag{E11}$$

with potential strengths $U_0 > 0$ and $W_0 > 0$, the leading-order absorption exponent is obtained in closed form:

$$\kappa_\alpha(\rho) = \sqrt{\pi}\frac{m_\alpha W_0}{\hbar^2 k_\alpha} R_W e^{-\rho^2/R_W^2}, \tag{E12}$$

depending only on the modulus of $\boldsymbol{\rho}$. Corresponding expressions are obtained for $\phi_\alpha$.

Within the Gaussian approximation, the reaction cross section can be evaluated in closed form. As shown in Ref. [42], the key point is to consider the continuity equation of the distorted waves from which one derives the relation

$$\begin{aligned}\sigma_{\mathrm{abs}}^{(\alpha)} &= -\frac{2m_\alpha}{\hbar^2 k_\alpha}\int d^3r |\chi_\alpha^{(+)}(\mathbf{k}_\alpha,\mathbf{r})|^2 W_\alpha(\mathbf{r}) \\ &= \int d^2\rho (1 - e^{-2\kappa_\alpha(\boldsymbol{\rho})}).\end{aligned} \tag{E13}$$

For a Gaussian $W(r)$, the integration can be performed analytically. As anticipated before, the result may be expressed indeed in a form resembling in structure the black disk expression

$$\sigma_{\mathrm{abs}}^{(\alpha)}(\sqrt{s_\alpha}) = \pi R_{\mathrm{abs}}^2(\sqrt{s_\alpha}), \tag{E14}$$

but where the effective absorption radius is related to the potential radius $R_W$ by the shape function $f(x)$

$$R_{\mathrm{abs}}^2(\sqrt{s_\alpha}) = f(\xi(W_\alpha, k_\alpha))R_W^2. \tag{E15}$$

The shape function is given analytically by

$$f(x) = \gamma + \log(x) + Ei(1,x), \tag{E16}$$

where $\gamma = 0.5772...$ denotes Euler's constant and $Ei(1,x)$ is an exponential integral. $f(x)$ is increasing steadily with $x$, vanishing at $x = 0$ and diverging logarithmically for $x \gg 1$. The argument

$$\xi(W,k) = \sqrt{\pi} k R_W \frac{W_0}{T_{\mathrm{cm}}}, \tag{E17}$$

depends on the reduced mass, the energy, and the absorption potential. $T_{\mathrm{cm}} = (\hbar k)^2/2m$ is the kinetic energy in the rest frame, and $kR_W \sim \ell_g$ corresponds to a grazing angular momentum with respect to the potential $W$. Hence, the absorption and the potential radius are relate in a nontrivial manner, changing with mass and energy. Results have been shown in Fig. 3.

## APPENDIX F: UNIT CROSS SECTION AND $\beta$-DECAY STRENGTHS

In this Appendix, we indicate the connection of the present formulation to the approach developed by Taddeucci *et al.* [14] for light-ion SCE reactions. As a side aspect, a schematic approach is derived from the full theory. In the Born approximation, the reaction cross section, Eq. (2), is simply given by the product of a kinematical factor and the modulus squared of the reaction amplitude $\mathcal{U}_{\alpha,\beta}$ in Eq. (16).

As shown in Sec. VI D, the distortion effects obtained in DWBA can be accounted for at small momentum transfer by means of the scaling function: $f_{\mathrm{BD}}(R_{\mathrm{abs}}, R, \sigma) = |1 - n_{\alpha\beta}|^2$.

Let us keep considering only $L = 0$ transitions, for both projectile and target, and only the central part of the nuclear interaction. Then, the SCE cross section, for small momentum transfer, can be recast in the form [see also Eqs. (30) and (31)]

$$\begin{aligned}d\sigma_{\alpha\beta} = {} & K_f(T_{\mathrm{lab}},\omega)(2S+1)|V_{\mathrm{ST}}^{(C)}(0)|^2 \left|b_{0SS}^{(ab)}\right|^2 \left|b_{0SS}^{(AB)}\right|^2 \\ & \times \exp\left[-\tfrac{1}{3}q_{\alpha\beta}^2(\langle r^2\rangle_a + \langle r^2\rangle_A)\right] f_{\mathrm{BD}}(R_{\mathrm{abs}}, R, \sigma),\end{aligned} \tag{F1}$$

where the expansion of the Bessel function in Eq. (A14) at small argument has been considered: $j_0(x) \approx 1 - 1/6\,x^2 \approx \exp(-1/6\,x^2)$. Thus, in the above equation, $\langle r^2\rangle_a$ and $\langle r^2\rangle_A$ denote the mean square radius of proton and neutron transition densities, respectively. The kinematical factor $K_f(T_{\mathrm{lab}},\omega)$ is given by

$$K_f(T_{\mathrm{lab}},\omega) = \frac{m_\alpha m_\beta}{(2\pi\hbar^2)^2}\frac{k_\beta}{k_\alpha}. \tag{F2}$$

It essentially depends on the energy loss $\omega = E_x - (M_A + M_a - M_B - M_b) = E_{\mathrm{tot}} - Q_{\mathrm{gs}}$, where $E_x = E_b^* + E_B^*$ is the total excitation energy.

The cross section can be rewritten as

$$d\sigma_{\alpha\beta} = F(q_{\alpha\beta},\omega)\sigma_U \left|b_{0SS}^{(ab)}\right|^2 \left|b_{0SS}^{(AB)}\right|^2, \tag{F3}$$

where we define a "unit" cross section, in analogy with what is usually done for SCE reactions involving light projectiles [14], as

$$\sigma_U = K_f(T_{\mathrm{lab}},0)|V_{\mathrm{ST}}^{(C)}(0)|^2 f_{\mathrm{BD}}(R_{\mathrm{abs}}, R, \sigma). \tag{F4}$$

The function $F$, mainly determining the shape of the cross section, is given by

$$F(q_{\alpha\beta},\omega) = \frac{K_f(T_{\mathrm{lab}},\omega)}{K_f(T_{\mathrm{lab}},0)}\exp\left[-\frac{1}{3}q_{\alpha\beta}^2(\langle r^2\rangle_a + \langle r^2\rangle_A)\right]. \tag{F5}$$

We note that the two equations above retrace the formalism developed in Ref. [14]. From Eq. (F5), it follows that $F(q_{\alpha\beta},\omega) \to 1$ for $(q_{\alpha\beta},\omega) \to (0,0)$, so that the proportionality coefficient between the SCE cross section and the product of the $\beta$ decay strengths relative to projectile and

target reduces to $\sigma_U$. In the plane-wave limit, $\sigma_U$ becomes

$$\sigma_U = K_f(T_{\rm lab}, 0)\left|V_{\rm ST}^{(C)}(0)\right|^2 \tag{F6}$$

so that it is characterized by a weak mass dependence [14]. On the other hand, the distortion factor $f_{\rm BD}$ may vary significantly with the system mass, as shown by Figs. 4 and 19.


[1] *The (p, n) Reaction and the Nucleon-Nucleon Force*, edited by C. D. Goodman *et al.* (Plenum, New York, 1980).
[2] M. Ichimura, H. Sakai, and T. Wakasa, Prog. Part. Nucl. Phys. **56**, 446 (2006).
[3] J. H. Thies, T. Adachi, M. Dozono, H. Ejiri, D. Frekers, H. Fujita, Y. Fujita, M. Fujiwara, E.-W. Grewe, K. Hatanaka *et al.*, Phys. Rev. C **86**, 044309 (2012).
[4] D. Frekers, P. Puppe, J. H. Thies, and H. Ejiri, Nucl. Phys. A **916**, 219 (2013).
[5] D. Frekers, T. Adachi, H. Akimune, M. Alanssari, B. A. Brown, B. T. Cleveland, H. Ejiri, H. Fujita, Y. Fujita, M. Fujiwara *et al.*, Phys. Rev. C **91**, 034608 (2015); S. Gales, Phys. Rev. Lett. **57**, 2375 (1986).
[6] Y. Fujita, B. Rubio, and W. Gelletly, Prog. Part. Nucl. Phys. **66**, 549 (2011).
[7] C. Brendel, P. von Neumann–Cosel, A. Richter, G. Schrieder, H. Lenske, H. H. Wolter, J. Carter, and D. Schüll, Nucl. Phys. A **477**, 162 (1988).
[8] C. Bérat, M. Buenerd, J. Chauvin, J. Y. Hostachy, D. Lebrun, P.Martin, J. Barrette, B. Berthier, B. Fernandez, and A. Miczaika *et al.*, Phys. Lett. B **218**, 299 (1989).
[9] H. Lenske, H. H. Wolter, and H. G. Bohlen, Phys. Rev. Lett. **62**, 1457 (1989).
[10] F. Cappuzzello *et al.*, Europhys. Lett. **65**, 766 (2004).
[11] F. Cappuzzello *et al.*, Phys. Lett. B **516**, 21 (2001).
[12] F. Cappuzzello, M. Cavallaro, C. Agodi, M. Bondi, D. Carbone, A. Cunsolo, and A. Foti, Eur. Phys. J. A **51**, 145 (2015).
[13] F. Cappuzzello *et al.*, Eur. Phys. J. A **54**, 72 (2018).
[14] T. N. Taddeucci *et al.*, Nucl. Phys. A **469**, 125 (1987).
[15] H. G. Bohlen *et al.*, Nucl. Phys. A **488**, 89 (1988).
[16] D. V. Bugg and C. Wilkin, Nucl. Phys. A **467**, 575 (1987).
[17] G. R. Satchler, *International Series of Monographs on Physics*, Direct Nuclear Reactions Vol. 68 (Clarendon, Oxford, UK, 1983).
[18] M. A. Franey and W. G. Love, Phys. Rev. C **31**, 488 (1985).
[19] F. Hofmann and H. Lenske, Phys. Rev. C **57**, 2281 (1998).
[20] A. R. Edmonds, *Angular Momentum in Quantum Mechanics* (Princeton University Press, Princeton, NJ, 1975).
[21] D. T. Khoa, W. von Oertzen, and H. G. Bohlen, Phys. Rev. C **49**, 1652 (1994).
[22] T. Wu and T. Ohmura, *Quantum Theory of Scattering* (Prentice-Hall, Englewood, NJ, 1962).
[23] G. N. Watson, *A Treatise on the Theory of Bessel Functions*, 2nd ed. (Cambridge University Press, Cambridge, UK, 1966).
[24] M. L. Goldberger and K. M. Watson, *Collision Theory* (Wiley, New York, 1967).
[25] P. E. Hodgson, *The Optica Model of Elastic Scattering* (Clarendon Press, New York, 1962).
[26] P. E. Hodgson, *Nuclear Heavy Ion Reactions* (Clarendon Press, Oxford, UK, 1978).
[27] M. Bondí, Ph.D. thesis, University of Catania, Italy, 2014.
[28] N. Tsoneva and H. Lenske, Phys. At. Nucl. **79**, 885 (2016).
[29] R. Machleidt, K. Holinde, and C. Elster, Phys. Rep. **149**, 1 (1987).
[30] G. Audi, F. G. Kondev, M. Wang, W. J. Huang, and S. Naimi, Chin. Phys. C **41**, 030001 (2017).
[31] F. T. Baker, L. Bimbot, C. Djalali, C. Glashausser, H. Lenske, W. G. Love, M. Morlet, E. Tomasi-Gustafsson, J. Van de Wiele, J. Wambach, and A. Willis, Phys. Rep. **289**, 235 (1997).
[32] C. Mahaux and H. Ngo, Nucl. Phys. A **378**, 205 (1982).
[33] http://www.nndc.bnl.gov/wallet/.
[34] F. J. Eckle, H. Lenske, G. Eckle, G. Graw, R. Hertenberger, H. Kader, H. J. Maier, F. Merz, H. Nann, P. Schiemenz, and H. H. Wolter, Nucl. Phys. A **506**, 159 (1990).
[35] F. J. Eckle, H. Lenske, G. Eckle, G. Graw, R. Hertenberger, H. Kader, F. Merz, H. Nann, P. Schiemenz, and H. H. Wolter, Phys. Rev. C **39**, 1662 (1989).
[36] W. G. Love and M. A. Franey, Phys. Rev. C **24**, 1073 (1981); **27**, 438(E) (1983).
[37] Y. Nagashima, J. Schimizu, T. Nakagawa, Y. Fukuchi, W. Yokota, K. Furuno, M. Yamanouchi, S. M. Lee, N. X. Dai, T. Mikumo, and T. Motobayashi, Phys. Rev. C **33**, 176 (1986).
[38] F. Cappuzzello *et al.*, Nucl. Phys. A **739**, 30 (2004).
[39] M. Sasano, G. Perdikakis, R. G. T. Zegers, S. M. Austin, D. Bazin, B. A. Brown, C. Caesar, A. L. Cole, J. M. Deaven, N. Ferrante *et al.*, Phys. Rev. C **86**, 034324 (2012).
[40] A. Bohr and B. Mottelsen, *Nuclear Structure* (W. A. Benjamin, New York, 1969), Vol. 1.
[41] C. J. Joachain, *Quantum Collision Theory* (North-Holland, Amsterdam, 1984).
[42] H. Lenske and P. Kienle, Phys. Lett. B **647**, 82 (2007).